PLASTIC-DAMAGE SMEARED CRACK MODEL TO SIMULATE THE BEHAVIOUR OF STRUCTURES MADE BY CEMENT BASED MATERIALS

A. Edalat Behbahani*[1], J. A. O. Barros[1], A. Ventura-Gouveia[2]

[1]ISISE, Dep. Civil Eng., School of Engineering, University of Minho, Guimarães, Portugal

[2]ISISE, Dep. Civil Eng., School of Technology and Management of Viseu, Polytechnic Institute of Viseu, Viseu, Portugal

ABSTRACT

This work proposes a constitutive model to simulate nonlinear behaviour of cement based materials subjected to different loading paths. The model incorporates a multidirectional fixed smeared crack approach to simulate crack initiation and propagation, whereas the inelastic behaviour of material between cracks is treated by a numerical strategy that combines plasticity and damage theories. For capturing more realistically the shear stress transfer between the crack surfaces, a softening diagram is assumed for modelling the crack shear stress versus crack shear strain. The plastic-damage model is based on the yield function, flow rule and evolution law for hardening variable, and includes an explicit isotropic damage law to simulate the stiffness degradation and the softening behaviour of cement based materials in compression. This model was implemented into the FEMIX computer program, and experimental tests at material scale were simulated to appraise the predictive performance of this constitutive model. The applicability of the model for simulating the behaviour of reinforced concrete shear wall panels submitted to biaxial loading conditions, and RC beams failing in shear is investigated.

KEYWORDS: FEM analysis, Fixed smeared crack model, Elasto-plasticity, Isotropic damage, Shear strengthening

1. INTRODUCTION

During the last decades several constitutive models have been developed in an attempt of capturing the quite sophisticated behaviour of cement based materials when submitted to multi-stress fields. To simulate the complex functioning of the structures formed by these materials, those constitutive models are in general implemented in computer programs based on the finite element method (FEM) [1-4]. Getting reliable FEM-based simulations is still a

* Author to whom correspondence should be send (aliedalatbehbahani@gmail.com)

challenge due to the complexity of concrete behaviour associated to the cracking in tension and crushing in compression. Experimental tests demonstrate that concrete behaviour in tension is brittle, and after cracking initiation concrete develops a softening behaviour with a decay of tensile capacity with the widening of the cracking process. This crack opening process is followed by a decrease of crack shear stress transfer due to the deterioration of aggregate interlock. Concrete in compression also demonstrates a pronounced nonlinear behaviour with an inelastic irreversible deformation. In the pre-peak stage of concrete response in uniaxial compression, a nonlinear stage is observed, whose amplitude depends of the concrete strength class, followed by a softening stage where brittleness is also dependent of the strength class. The complexity of concrete behaviour increases when submitted to multiaxial stress field that is the current situation of the major reinforced concrete (RC) structures.

The elasto-plasticity (generally abbreviated as plasticity) [5], the nonlinear fracture mechanics [6] and the continuum damage mechanics (CDM) [7] are the frequently used approaches to simulate the behaviour of concrete structures. The elasto-plasticity theory is preferentially used for modelling the multiaxial behaviour of concrete, since the concept of failure criterion defines the strength capacity of a material when submitted to a generic stress field. The models based on elasto-plasticity alone fail to address the damage process due to crack initiation and propagation, therefore the experimentally observed stiffness degradation of the material is not captured accurately by using exclusively the elasto-plasticity theory [8, 9]. In fact, the recent numerical models complement the elasto-plasticity theory with other approaches that provide a better interpretation of concrete behaviour in tension. Combining the elasto-plasticity theory with CDM [8-15], and with the nonlinear fracture mechanics [6, 16] are alternatives that have been explored.

The theoretical framework of the CDM is based on the gradual reduction of the elastic stiffness. The damage is defined as the loss of strength and stiffness of the material when subjected to a certain loading process. However the CDM alone is not able to reproduce the irreversible (permanent) deformation of the concrete that is pronounced in the case of high confined compressive loading [10, 11]. Therefore plasticity and damage theories are being merged in an attempt of constituting reliable approaches capable of simulating the strength and stiffness degradation and occurrence of irreversible deformations. The plastic-damage models usually adopt the flow theory of plasticity based on isotropic hardening combined with either the isotropic, or anisotropic damage formulations [8], and different types of coupling strategies of the two theories are available [13]. Anisotropic damage models consider a damage tensor to account for micro-cracking in different directions, but the adoption of this approach is limited due to the high level of sophistication when it is combined with the plasticity [14]. The isotropic, scalar, damage models, on the other hand, are very often implemented in combination with the plasticity theory [8, 11, 12, 15], since they assume a state of damage equally distributed in all the material directions by means of a scalar measure. A realistic prediction of concrete damage process requires the adoption of at least two damage variables, one for tension and another for compression [8-15].

Another possibility of overcoming limitations of the plasticity theory is coupling a fracture approach to the elasto-plasticity [6, 16]. In this class of models, the theory of plasticity is used to deal with the elasto-plastic behaviour of material under compression, whereas various fracture theories can be used to simulate the cracking behaviour. The present study proposes a constitutive model that belongs to this category, since the process of cracking initiation and propagation is accounted by a multi-directional fixed smeared crack approach, while the inelastic compressive behaviour of the material between cracks is simulated by a stress-based plasticity model. The plasticity model is described with the help of a pressure-sensitive yield surface inspired on the work of Willam and Warnke [17]. Some of the models based on classical plasticity simulate directly the material softening/hardening behaviour by including softening/hardening functions in the equation of the yield surface [18-21]. However, in the proposed constitutive model the plasticity part is maintained in hardening phase to only account for the development of irreversible strains and volumetric strain in compression, whereas the strain softening and stiffness degradation of the material under compression is controlled by an isotropic strain base damage model.

In this work the main objective is to develop an efficient model capable of simulating the nonlinearities of cement based materials, like concrete, subjected to several loading paths. For this purpose a brief description of the already existing multi-directional fixed smeared crack approach (SC) is made [22, 23]. Then, a plasticity-damage model is proposed to consider the inelastic deformation of material between the cracks, and its coupling with the SC was implemented in the FEMIX FEM-based computer program [24]. To evaluate the performance of the model and to evidence the interaction between cracking and plasticity-damage parts of the model, some numerical tests at material level are executed and the obtained results are discussed. The predictive performance of the model was then extended by simulating: shear wall panel tests; an experimental program composed of T cross section RC beams shear strengthened with different configurations of carbon fibre reinforced polymer (CFRP) laminates applied according to the Near Surface Mounted (NSM) technique. Based on the numerical simulations of these experimental tests, the potentialities of the proposed model are discussed.

2. MODEL DESCRIPTION

2.1 – Multi-directional fixed smeared crack (SC) model

Modelling cracked materials using a smeared approach is usually based on the decomposition of the total incremental strain vector, $\Delta\underline{\varepsilon}$, into an incremental crack strain vector, $\Delta\underline{\varepsilon}^{cr}$, and an incremental concrete strain vector, $\Delta\underline{\varepsilon}^{co}$, as proposed by De Borst [25], $\Delta\underline{\varepsilon} = \Delta\underline{\varepsilon}^{co} + \Delta\underline{\varepsilon}^{cr}$. Assembling in $\Delta\underline{\varepsilon}^{cr}$ the deformational contribution of the sets of smeared cracks that can be formed (according to a crack opening criterion) in an integration point (IP), the constitutive

law of the multi-directional fixed smeared crack (SC) model is obtained. In the present section the SC model is briefly discussed and its presentation is restricted to plain stress state and at the domain of an IP.

For the present stage of the model description, it is assumed that material between cracks develops linear elastic behaviour, therefore the $\Delta\underline{\varepsilon}^{co}$ is the incremental elastic strain vector ($\Delta\underline{\varepsilon}^{co} = \Delta\underline{\varepsilon}^{e}$). To simulate the plastic response of material in compression, the $\Delta\underline{\varepsilon}^{co}$ should also include the plastic part of the material deformation, $\Delta\underline{\varepsilon}^{co} = \Delta\underline{\varepsilon}^{e} + \Delta\underline{\varepsilon}^{p}$, which will be discussed in the next section.

The constitutive law for the elastic-cracked material can be, therefore, written as:

$$\Delta\underline{\bar{\sigma}} = \underline{D}^{e} \left(\Delta\underline{\varepsilon} - \Delta\underline{\varepsilon}^{cr}\right) \tag{1}$$

being $\Delta\underline{\bar{\sigma}} = \{\Delta\bar{\sigma}_1, \Delta\bar{\sigma}_2, \Delta\bar{\tau}_{12}\}$ the incremental stress vector induced into the material due to $\Delta\underline{\varepsilon} = \{\Delta\varepsilon_1, \Delta\varepsilon_2, \Delta\gamma_{12}\}$ and considering the constitutive matrix of the intact material, $\underline{D}^{e}$.

The $\Delta\underline{\varepsilon}^{cr}$ is obtained from the incremental local crack strain vector, $\Delta\underline{\varepsilon}_{\ell}^{cr}$:

$$\Delta\underline{\varepsilon}^{cr} = \left[\underline{T}^{cr}\right]^{T} \Delta\underline{\varepsilon}_{\ell}^{cr} \tag{2}$$

where:

$$\Delta\underline{\varepsilon}_{\ell}^{cr} = \left[\Delta\varepsilon_{n,1}^{cr}\ \Delta\gamma_{t,1}^{cr} \ldots \Delta\varepsilon_{n,i}^{cr}\ \Delta\gamma_{t,i}^{cr} \ldots \Delta\varepsilon_{n,m}^{cr}\ \Delta\gamma_{t,m}^{cr}\right]^{T} \tag{3}$$

includes normal ($\Delta\varepsilon_n^{cr}$) and tangential ($\Delta\gamma_t^{cr}$) crack strain components of the *m* cracks that can be formed in an IP, and $\underline{T}^{cr}$ is the matrix that transforms the stress components from the coordinate system of the finite element to the local coordinate system of each crack (a subscript ℓ is used to identify entities in the local crack coordinate system). If *m* cracks occur at an IP:

$$\underline{T}^{cr} = \left[\underline{T}_1^{cr} \ldots \underline{T}_i^{cr} \ldots \underline{T}_m^{cr}\right]^{T} \tag{4}$$

The transformation matrix of generic *i*th crack, $\underline{T}_i^{cr}$, is obtained by having orientation of the *i*th crack, θ_i, that is the angle between x_1 axis and the vector perpendicular to the *i*th crack [22].

At the crack zone (damage material) of an IP, the opening and sliding process is governed by the following crack constitutive relationship:

$$\Delta\underline{\sigma}_{\ell}^{cr} = \underline{D}^{cr} \Delta\underline{\varepsilon}_{\ell}^{cr} \tag{5}$$

where $\Delta\underline{\sigma}_{\ell}^{cr}$ is the vector of the incremental crack stress in the crack coordinate system with the contribution of normal, $\Delta\sigma_n^{cr}$, and tangential components, $\Delta\tau_t^{cr}$:

$$\Delta\underline{\sigma}_{\ell}^{cr} = \left[\Delta\sigma_{n,1}^{cr}\ \Delta\tau_{t,1}^{cr} \ldots \Delta\sigma_{n,i}^{cr}\ \Delta\tau_{t,i}^{cr} \ldots \Delta\sigma_{n,m}^{cr}\ \Delta\tau_{t,m}^{cr}\right]^{T} \tag{6}$$

where $\underline{D}^{cr}$ is the matrix that includes the constitutive law of the *m* active cracks, i.e., the ones not completely closed. Accordingly the constitutive law of *i*th generic crack, $\underline{D}_i^{cr}$, is given:

$$\underline{D}_i^{cr} = \begin{bmatrix} D_n^{cr} & 0 \\ 0 & D_t^{cr} \end{bmatrix} \tag{7}$$

where D_n^{cr} and D_t^{cr} represent, respectively, the stiffening/softening modulus corresponding to fracture mode I (normal), and fracture mode II (shear), of the *i*th crack.

At the IP the equilibrium condition is assured by imposing the following condition:

$$\Delta\underline{\sigma}_{\ell}^{cr} = \underline{T}^{cr}\Delta\underline{\bar{\sigma}} \tag{8}$$

In the course of the implementation of the constitutive model, it is assumed that at a certain loading step, n, the stress and strain quantities are known, and the local crack variables are updated as well. At the onset of the next loading step, $n+1$, Eq. (8) must be accomplished:

$$\underline{\sigma}_{\ell,n+1}^{cr} = \underline{T}_{n+1}^{cr}\ \underline{\bar{\sigma}}_{n+1} \tag{9}$$

Including Eqs. (1), (2) and (5) into Eq. (9), and taking into account that $\underline{\sigma}_{\ell,n+1}^{cr} = \underline{\sigma}_{\ell,n}^{cr} + \Delta\underline{\sigma}_{\ell,n+1}^{cr}$ and $\underline{\bar{\sigma}}_{n+1} = \underline{\bar{\sigma}}_n + \Delta\underline{\bar{\sigma}}_{n+1}$, yields, after some arrangements, in:

$$\underline{\sigma}_{\ell,n}^{cr} + \underline{D}_{n+1}^{cr}\Delta\underline{\varepsilon}_{\ell,n+1}^{cr} - \underline{T}_{n+1}^{cr}\underline{\bar{\sigma}}_n - \underline{T}_{n+1}^{cr}\underline{D}^{e}\,\Delta\underline{\varepsilon}_{n+1} + \underline{T}_{n+1}^{cr}\underline{D}^{e}\left[\underline{T}_{n+1}^{cr}\right]^{T}\Delta\underline{\varepsilon}_{\ell,n+1}^{cr} = \underline{0} \tag{10}$$

The Newton-Raphson method is used to solve this system of nonlinear equations, where the unknowns are the components of $\Delta\underline{\varepsilon}_{\ell,n+1}^{cr}$. After obtaining $\Delta\underline{\varepsilon}_{\ell,n+1}^{cr}$, the $\Delta\underline{\varepsilon}_{n+1}^{cr}$ and $\Delta\underline{\sigma}_{\ell,n+1}^{cr}$ are determined from Eqs. (2) and (5), respectively, and finally $\Delta\underline{\bar{\sigma}}_{n+1}$ is calculated from Eq. (1).

The crack initiation is governed by the Rankin failure criterion that assumes a crack occurs when the maximum principal tensile stress in a IP attains the concrete tensile strength, f_{ct}, under an assumed tolerance. After crack initiation, the relationship between the normal stress and the normal strain in the crack coordinate system, i.e. $\sigma_n^{cr} - \varepsilon_n^{cr}$, is simulated via the trilinear diagram represented in Fig. 1 [22]. Normalized strain, $\xi_i\,(i=1,2)$, and stress, $\alpha_i\,(i=1,2)$, parameters are used to define the transition points between linear segments, being G_f^{I} the fracture energy mode I, while l_b is the characteristic length (crack bandwidth) used to assure that the results of a material nonlinear analysis is not dependent of the refinement of the finite element mesh.

The model considers shear behaviour of the cracked concrete according to two methods:

1) using an incremental crack shear stress shear strain approach based on a shear retention factor, β. According to this approach the fracture mode II modulus, D_t^{cr}, is simulated as:

$$D_t^{cr} = \frac{\beta}{1-\beta} G_c \tag{11}$$

where G_c is the concrete elastic shear modulus, while the shear retention factor , β, can be a constant value or, alternatively, as a function of current crack normal strain, ε_n^{cr}, and of ultimate crack normal strain, $\varepsilon_{n,u}^{cr}$, such as:

$$\beta = \left(1 - \frac{\varepsilon_n^{cr}}{\varepsilon_{n,u}^{cr}}\right)^{P_1} \tag{12}$$

being the exponent P_1 a parameter that defines the decrease rate of β with increasing ε_n^{cr}.

2) adopting a $\tau_t^{cr} - \gamma_t^{cr}$ softening law to simulate more correctly the shear stress transfer during the crack opening process, which allows better predictions in terms of load carrying capacity, deformability, and crack pattern of RC elements failing in shear [23]. The adopted shear softening law is represented in Fig. 2, and can be formulated by the following equation [23]:

$$\tau_t^{cr} = \begin{cases} D_{t,1}^{cr}\, \gamma_t^{cr} & 0 < \gamma_t^{cr} \le \gamma_{t,p}^{cr} \\ \tau_{t,p}^{cr} - \dfrac{\tau_{t,p}^{cr}}{\gamma_{t,u}^{cr} - \gamma_{t,p}^{cr}} \left(\gamma_t^{cr} - \gamma_{t,p}^{cr}\right) & \gamma_{t,p}^{cr} < \gamma_t^{cr} \le \gamma_{t,u}^{cr} \\ 0 & \gamma_t^{cr} > \gamma_{t,u}^{cr} \end{cases} \tag{13}$$

where $\tau_{t,p}^{cr}$ is the crack shear strength (shear stress at peak), $\gamma_{t,p}^{cr} = \tau_{t,p}^{cr} / D_{t,1}^{cr}$ is the crack shear strain at peak, and $\gamma_{t,u}^{cr}$ is the ultimate crack shear strain:

$$\gamma_{t,u}^{cr} = \frac{2G_{f,s}}{\tau_{t,p}^{cr}\, l_b} \tag{14}$$

being $G_{f,s}$ the fracture energy corresponding to fracture mode II, and l_b the crack bandwidth that is assumed to be equal to the one adopted to simulate the fracture mode I. Since no dedicated research is available on the process of determining the crack band width parameter that bridges crack shear slide with shear deformation in the smeared shear crack band, it was decided to adopt the same strategy for the crack band width regardless the type of fracture process. This decision has, at least, the advantage of assuring the same results regardless the mesh refinement, which is not assured when using the concept of shear retention factor in structures failing in shear. The inclination of the hardening branch of diagram, $D_{t,1}^{cr}$ (see Fig. 2), is introduced according to (11) where β is set as a constant value in the range $]0,1[$. More details corresponding to the crack shear softening diagram can be found elsewhere [23].

Fig. 3 represents a schematic representation of the crack shear stress-shear strain diagram for the incremental approach based on shear retention factor (Eq. (11) and Eq. (12)). It is verified that with the increase of γ_t^{cr} the crack shear modulus, D_t^{cr}, decreases but the crack shear stress, τ_t^{cr}, increases up to attain a maximum that depends on the parameters considered for the Eq. (12). This value can be much higher than the concrete shear strength according to available experimental data and design guidelines. For RC elements failing in bending the maximum value of γ_t^{cr} is relatively small, therefore simulating shear stress degradation with the evolution of γ_t^{cr} has not relevant impact of the predictive performance of the simulations. However, in RC structures failing in shear, the adoption of a constitutive law capable of simulating the crack shear stress degradation, as the one adopted in the present work, is fundamental for the predictive performance. The computing time consuming and the convergence stability of the incremental and iterative procedure of the model when adopting softening diagrams for simulating all the fracture processes are, however, increased, therefore shear softening approach is only recommended when shear is the governing failure mode.

2.2 – Plastic-damage multi-directional fixed smeared crack (PDSC) model

The SC model described in the section 2.1 is now extended in order to simulate the inelastic behaviour of cement based materials in a compression-compression and compression-tension stress fields. For this purpose a plastic-damage approach is coupled with the SC model, deriving a model herein designated as plastic-damage multi-directional fixed smeared crack (PDSC) model, which is capable of simulating the nonlinear behaviour of cement based materials due to both cracking and inelastic deformation in compression.

2.2.1 – Damage concept in the context of plastic-damage model

To demonstrate the process of damage evolution in compression when an isotropic damage model is applied to simulate strength and stiffness degradation in compression, a simple bar loaded in compression is presented. This problem is similar to the case of the bar under tension proposed by Kachanov [26]. Consider a bar made by cement based materials and exposed to a certain level of damage due to uniaxial compressive force, N, as illustrated in Fig. 4a [14]. The total cross-sectional area of the bar in damaged, nominal, status is denoted by A, then the stress developed on this area is defined as $\sigma = N/A$, herein designated as nominal stress. Due to the thermo-hygrometric effects during the curing process of cement based materials, voids and micro-cracks are formed even before these materials have been loaded by external loads [20]. However, the impact of these "defects" in terms of stiffness and strength of the material can be neglected, and the degeneration of the micro- into meso- and macro cracks is generally a gradual damage process depending on the evolution of the external loading conditions. Let's assume the variable A^D represents the area

corresponding to these defects (meso- and macro cracks) (Fig. 4b). According to the principle of isotropic damage approach, a scalar measure, d_c, is defined to represent this damage level in total cross-sectional area (A), such that:

$$d_c = \frac{A_D}{A} \tag{15}$$

that can take values from 0 to 1. The state $d_c = 0$ implies the area of A is intact, while $d_c = 1$ denotes the area of A is completely damaged.

A fictitious undamaged, effective, area of $\bar{A}$, is defined by removing all the damage regions from the area of A ($\bar{A} = A - A_D = (1 - d_c)A$), then the uniaxial stress developed on the area $\bar{A}$, $\bar{\sigma} = N/\bar{A}$, is denoted as effective stress (Fig. 4c). Since the applied force on both damaged and undamaged areas is N, then the following relation holds between the uniaxial stress at damaged (nominal), σ, and undamaged (effective), $\bar{\sigma}$, configurations:

$$\sigma = (1 - d_c)\bar{\sigma} \tag{16}$$

By extending this concept for a multidimensional stress field, the relation between the nominal stress vector ($\underline{\sigma}$), and the effective stress vector ($\underline{\bar{\sigma}}$) for isotropic damage models can be expressed as:

$$\underline{\sigma} = (1 - d_c)\underline{\bar{\sigma}} \tag{17}$$

The present study adopts a stress based plasticity model formulated in effective stress space in combination with an isotropic damage model. The resultant plastic-damage approach is meant to utilize for modelling inelastic deformation of material under compression.

An important assumption of the proposed plastic-damage model is to define the stage that damage initiation takes place. In this study the damage threshold was assumed based on the phenomenological interpretation of the behaviour of current concrete under compressive loading. Fig. 5a demonstrates the three distinct consecutive stages of cracking that can be identified in concrete under uniaxial compressive load, based on initiation and propagation of cracks [27]:

Stage I - below ≈30% of the peak stress. The formation of internal cracks at this stage is negligible, and the stress-strain response of the material may be assumed as linear;

Stage II - between ≈30% and ≈100% of the peak stress. At the beginning of this stage the internal cracks initiate and propagate at the interface zone and new micro-cracks develop. Around 60% of the peak stress, the micro-cracks at the cementitious matrix start to develop randomly over volume of the material. At approximately 80% up to 100% of the peak stress, all the small internal cracks become unstable and start to localize into major cracks;

Stage III - after peak load. At this stage the major cracks continuously propagate, although the applied load is reducing.

In this study damage initiation is assumed to be related to development of the major cracks formed after the peak load. Then evolution of the damage through the stage II is considered to be null ($d_c = 0$), and nonlinear behaviour of the

current concrete in this stage is reproduced by only a plasticity model. At the stage III the plasticity model is responsible for simulating irreversible plastic deformation and inelastic volumetric expansion of the material whereas the isotropic damage model deals with strength and stiffness degradation of the material due to formation of the major cracks. Fig. 5b demonstrates the schematic representation of the damage evolution at the proposed plastic-damage model for the three stages of cracking in uniaxial compression.

It is noted the statement of "damage" in the text intends to simulate the inelastic behaviour of concrete in compression by using a plastic-damage model, while cracking formation and propagation is simulated by a SC model. Therefore, if concrete is cracked and concrete between cracks experience inelastic deformation in compression, both models are coupled.

2.2.2 – Constitutive relationship for PDSC model

For modelling of a cracked member with material between cracks in compression, the term $\Delta\underline{\varepsilon}^{co}$ is further decomposed into its elastic, $\Delta\underline{\varepsilon}^{e}$, and plastic parts, $\Delta\underline{\varepsilon}^{p}$, ($\Delta\underline{\varepsilon}^{co} = \Delta\underline{\varepsilon}^{e} + \Delta\underline{\varepsilon}^{p}$), thereby the incremental constitutive relation for the PDSC model is given by:

$$\Delta\underline{\bar{\sigma}} = \underline{D}^{e}\left(\Delta\underline{\varepsilon} - \Delta\underline{\varepsilon}^{p} - \Delta\underline{\varepsilon}^{cr}\right) \tag{18}$$

where the incremental crack strain vector, $\Delta\underline{\varepsilon}^{cr}$, is evaluated by the SC model described in section 2.1. A stress based plasticity model formulated in effective stress space, i.e. without considering damage, is responsible for the evaluation of $\Delta\underline{\varepsilon}^{p}$. The plasticity model assumes that plastic flow occurs on the undamaged material between the damaged regions formed during the strain softening compression stage of the material. Then the effective stress state obtained according to Eq. (18) needs to be mapped into nominal stress space according to the principle of CDM. This mapping process should distinguish the tensile from the compressive stress components, since the damage is only applied to these last ones. Ortiz [28] proposed the split of the effective stress vector, $\underline{\bar{\sigma}}$, into positive (tensile) and negative (compressive) components to adopt different scalar damage variables for tension and compression. Such operation is given by:

$$\underline{\bar{\sigma}} = \underline{\bar{\sigma}}^{+} + \underline{\bar{\sigma}}^{-}, \qquad \underline{\bar{\sigma}}^{+} = \sum_{i}\left\langle \bar{\sigma}^{i}\right\rangle \underline{P}^{i} \otimes \underline{P}^{i} \tag{19}$$

where $\underline{\bar{\sigma}}^{+}$ and $\underline{\bar{\sigma}}^{-}$ are the positive and the negative parts of the effective stress vector, respectively, and $\bar{\sigma}^{i}$ is the i^{th} principal stress extracted from vector $\underline{\bar{\sigma}}$, and $\underline{P}^{i}$ is the normalized eigenvector associated with the i^{th} principal stress ($\bar{\sigma}^{i}$). The symbol $\langle . \rangle$ denotes Macaulay bracket function operating as $\langle x\rangle = \left(x + |x|\right)/2$.

The compressive damage scalar, d_c, must affect only the negative part of the effective stress vector, i.e. $\underline{\bar{\sigma}}^{-}$, therefore a similar approach to Eq. (17) gives the nominal stress vector, such as:

$$\underline{\sigma} = \underline{\bar{\sigma}}^{+} + (1 - d_c)\,\underline{\bar{\sigma}}^{-} \tag{20}$$

235

236 **2.2.3 – Plasticity model in effective stress space**

237 The plastic strain vector, $\Delta\underline{\varepsilon}^{p}$, is evaluated by a time-independent plasticity model that is defined by four entities: yield
238 function (yield surface); flow rule; evolution law for the hardening variable; and condition for defining loading-
239 unloading process. In this study the yield function, f, was derived from the five-parameter Willam and Warnke (W-
240 W) failure criterion [17] (the details of this process are in the Annex A), which shows a good ability to represent the
241 experimental results of cement based materials [17, 29], and also satisfies all the requirements of being smooth, convex,
242 pressure dependent, and curved in the meridian plain.
243 The equation of this yield function is:

$$f\left(\underline{\bar{\sigma}};\, \bar{\sigma}_c(\tilde{\epsilon}_c)\right) = \left[\left(\frac{\bar{I}_1}{\sqrt{3}\,c} - \frac{\sqrt{2}\,b}{c}\sqrt{\bar{J}_2}\right)\bar{\sigma}_c(\tilde{\epsilon}_c) - \frac{2a}{c}\bar{J}_2\right]^{1/2} - \bar{\sigma}_c(\tilde{\epsilon}_c) = 0 \tag{21}$$

244 where $\bar{I}_1$ is the first invariant of the effective stress tensor, $\bar{J}_2$ is the second invariant of the deviatoric effective stress
245 tensor, and $\bar{\theta}$ is the angle of similarity, also known as Lode angle:

$$\bar{I}_1 = \underline{\bar{\sigma}}_{ii}; \quad \bar{J}_2 = \tfrac{1}{2}\underline{\bar{S}}_{ij}\underline{\bar{S}}_{ij}; \quad \bar{\theta} = \frac{1}{3}\arccos\left(\frac{3\sqrt{3}}{2}\frac{\bar{J}_3}{\bar{J}_2^{3/2}}\right) \tag{22}$$

246 where $\underline{\bar{\sigma}}_{ij,(i,j=1,2,3)}$ is the effective stress tensor, $\underline{\bar{S}}_{ij} = \underline{\bar{\sigma}}_{ij} - \underline{\delta}_{ij}\,\bar{I}_1/3$ is the deviatoric effective stress tensor, and
247 $\bar{J}_3 = \tfrac{1}{3}\underline{\bar{S}}_{ij}\underline{\bar{S}}_{jk}\underline{\bar{S}}_{ki}$ is the third invariant of the deviatoric effective stress tensor. The variables *a*, *b* and *c* are the scalars
248 used to interpolate the current yield meridian between the tensile and compressive meridians, as described in detail in
249 the Annex A.
250 The term $\bar{\sigma}_c(\tilde{\epsilon}_c)$ is the hardening function depending on the hardening parameter ($\tilde{\epsilon}_c$). The hardening parameter is a
251 scalar measure used to characterize the plastic state of the material under compressive stress field. Therefore $\tilde{\epsilon}_c$ is an
252 indicator of the degree of inelastic deformation the material has experienced during the loading history. The evolution
253 of the yield surface during the plastic flow is governed by $\tilde{\epsilon}_c$. As long as $\tilde{\epsilon}_c$ is null, no inelastic deformation occurred,
254 and $f(\underline{\bar{\sigma}};\, \bar{\sigma}_c(\tilde{\epsilon}_c = 0)) = f(\underline{\bar{\sigma}};\, \alpha_0\, f_c) = 0$ corresponds to the initial yield surface (α_0 is a material constant to define the
255 beginning of the nonlinear behaviour in uniaxial compressive stress-strain test, and f_c is the compressive strength).
256 When the effective stress state reaches to the yield surface at generic stage (*i*) of yielding process, $f_i \geq 0$, plastic strains
257 are developed , being its increment evaluated by a flow rule:

$$\Delta \underline{\varepsilon}^{p} = \Delta\lambda \frac{\partial g}{\partial \underline{\bar{\sigma}}} \tag{23}$$

where g is a scalar function, called plastic potential function, and $\Delta\lambda$ is the non-negative plastic multiplier. In the present version of the model, $g = f$ was assumed [30], therefore associate plasticity is adopted for preserving the symmetry of the tangent stiffness matrix for the elasto-plastic model.

The state of hardening parameter, $\tilde{\epsilon}_c$, during the plastic flow is changed according to the following evolution law [31]:

$$\Delta\tilde{\epsilon}_c = -\Delta\lambda \frac{\partial f}{\partial \bar{\sigma}_c} \tag{24}$$

The yield function (f) and plastic multiplier ($\Delta\lambda$) at any stage of loading and unloading paths are constrained to follows Kuhn-Tucker conditions:

$$\Delta\lambda \geq 0, \quad f(\underline{\bar{\sigma}}, \tilde{\epsilon}_c) \leq 0, \ \Delta\lambda\, f(\underline{\bar{\sigma}}, \tilde{\epsilon}_c) = 0 \tag{25}$$

2.2.3.1 Hardening law

Compressive behaviour of the material in effective stress space is governed by the uniaxial hardening law of $\bar{\sigma}_c - \tilde{\epsilon}_c$ (Fig. 6a). The $\bar{\sigma}_c$ is the current uniaxial compressive stress in effective stress space, and the hardening parameter ($\tilde{\epsilon}_c$) is an equivalent plastic strain measure proportional to the plastic strain ($\underline{\varepsilon}^{p}$) developed in the material. Hardening parameter corresponding to total axial strain at compression peak stress ($\tilde{\epsilon}_{c1}$) is obtained such that:

$$\tilde{\epsilon}_{c1} = \varepsilon_{c1} - f_c / E \tag{26}$$

being ε_{c1} the total strain at compression peak stress.

In this study it is assumed that the compressive damage, d_c , is initiated at the plastic deformation corresponding to $\tilde{\epsilon}_{c1}$, i.e. if $\tilde{\epsilon}_c \leq \tilde{\epsilon}_{c1}$, then $d_c = 0$ (Fig. 6b). According to this assumption, the effective and nominal responses are identical for the domain of $\tilde{\epsilon}_c \leq \tilde{\epsilon}_{c1}$ (Eq. (17) assuming $d_c = 0$). Then $\bar{\sigma}_c - \tilde{\epsilon}_c$ for the domain of $\tilde{\epsilon}_c \leq \tilde{\epsilon}_{c1}$ can be directly obtained by experimental uniaxial stress-strain curves, which are in the nominal stress space, such relation was adopted according to the CEB-FIP (1993) model [32] as:

$$\bar{\sigma}_c(\tilde{\epsilon}_c) = f_{c0} + (f_c - f_{c0}) \left[\frac{2\tilde{\epsilon}_c}{\tilde{\epsilon}_{c1}} - \frac{(\tilde{\epsilon}_c)^2}{(\tilde{\epsilon}_{c1})^2} \right]^{1/2} \tag{27}$$

where f_{c0} is the uniaxial compressive strength at plastic threshold, i.e. $\bar{\sigma}_c(\tilde{\epsilon}_c = 0) = \alpha_0\, f_c$.

For $\tilde{\epsilon}_c > \tilde{\epsilon}_{c1}$, the damage takes place ($d_c > 0$), then the effective stresses cannot be determined by direct identifications from relevant uniaxial compressive stress-strain tests [11, 14]. For this domain ($\tilde{\epsilon}_c > \tilde{\epsilon}_{c1}$) and in order to reduce the

number of parameters required in the plasticity model it is assumed a hardening branch defined according to the following equation:

$$\bar{\sigma}_c(\tilde{\epsilon}_c) = \frac{f_c}{0.02 - \tilde{\epsilon}_{c1}}(\tilde{\epsilon}_c - \tilde{\epsilon}_{c1}) + f_c \tag{28}$$

A more elaborated version of Eq. (28) with the ability to define the inclination of the hardening phase is represented in Annex B, and the resultant response of the proposed model in cyclic uniaxial compressive test is discussed. Fig. 6a represents the hardening law ($\bar{\sigma}_c - \tilde{\epsilon}_c$) formulated in Eq. (27) and Eq. (28).

Based on Eq. (27) and Eq. (28), the stress-strain response of the model in effective stress space does not exhibit softening phase, which is in alignment with the results obtained by Abu Al-Rub and Kim [14].

2.2.3.2 System of nonlinear equations

Assuming the material is in uncracked stage, or eventually the former active cracks are completely closed, then the incremental crack strain is null, $\Delta\underline{\varepsilon}^{cr} = 0$, and the constitutive law of PDSC model, Eq. (18), is reduced to:

$$\Delta\underline{\bar{\sigma}} = \underline{D}^e(\Delta\underline{\varepsilon} - \Delta\underline{\varepsilon}^p) \tag{29}$$

Including Eq. (23) in Eq. (29), and taking into account that $\underline{\bar{\sigma}}_{n+1} = \underline{\bar{\sigma}}_n + \Delta\underline{\bar{\sigma}}_{n+1}$, yields:

$$\underline{\bar{\sigma}}_{n+1} - \left(\underline{\bar{\sigma}}_n + \underline{D}^e\,\Delta\underline{\varepsilon}_{n+1}\right) + \Delta\lambda_{n+1}\underline{D}^e\left(\frac{\partial f}{\partial\underline{\bar{\sigma}}}\right)_{n+1} = \underline{0} \tag{30}$$

where the subscript *n+1* represents the actual load increment of the incremental/iterative Newton-Raphson algorithm generally adopted in FEM-based material nonlinear analysis. The equations describing the yield function, Eq. (21), and the evolution law for hardening variable, Eq. (24), at loading increment $n+1$ are given as:

$$f(\underline{\bar{\sigma}}_{n+1};\ \bar{\sigma}_{c,n+1}(\tilde{\epsilon}_{c,n+1})) = 0 \tag{31}$$

$$\Delta\tilde{\epsilon}_{c,n+1} + \Delta\lambda_{n+1}\frac{\partial f_{n+1}}{\partial\bar{\sigma}_{c,n+1}} = 0 \tag{32}$$

The system of equations for the proposed plasticity model includes the Eqs. (30)-(32) that must be solved for set of the unknowns that are the effective stress vector, $\underline{\bar{\sigma}}_{n+1}$, and the plasticity internal variables, $\Delta\lambda_{n+1}$ and $\tilde{\epsilon}_{c,n+1}$. The return-mapping algorithm is used to solve this system of nonlinear equations [33]. The return-mapping algorithm is strain driven and basically consist of two steps; calculation of the elastic trial stress, elastic-predictor, and mapping back to the proper yield surface using a local iterative process, plastic-corrector. The details of the solution procedure of the system of nonlinear equations can be found elsewhere [34].

2.2.4 – Coupling the plasticity and the SC models

In this section the plasticity model, formulated in effective stress space, and the multi-directional smeared crack (SC) model are combined within an integrated approach in order to be capable of evaluating $\Delta\underline{\varepsilon}^{cr}$ and $\Delta\underline{\varepsilon}^{p}$ simultaneously at a generic integration point (IP). As indicated in section 2.1, the equilibrium condition for a cracked IP is assured when:

$$\underline{\sigma}_{\ell,n}^{cr} + \underline{D}_{n+1}^{cr}\Delta\underline{\varepsilon}_{\ell,n+1}^{cr} = \left[\underline{T}_{n+1}^{cr}\right]\left(\overline{\underline{\sigma}}_{n} + \Delta\overline{\underline{\sigma}}_{n+1}\right) \tag{33}$$

Introducing Eqs. (2), (18) and (23) into Eq. (33) yields after some arrangements in:

$$\underline{\sigma}_{\ell,n}^{cr} + \underline{D}_{n+1}^{cr}\Delta\underline{\varepsilon}_{\ell,n+1}^{cr} - \underline{T}_{n+1}^{cr}\overline{\underline{\sigma}}_{n} - \underline{T}_{n+1}^{cr}\underline{D}^{e}\,\Delta\underline{\varepsilon}_{n+1} + \underline{T}_{n+1}^{cr}\underline{D}^{e}\left[\underline{T}_{n+1}^{cr}\right]^{T}\Delta\underline{\varepsilon}_{\ell,n+1}^{cr} + \Delta\lambda_{n+1}\underline{T}_{n+1}^{cr}\underline{D}^{e}\left(\frac{\partial f}{\partial\overline{\underline{\sigma}}}\right)_{n+1} = \underline{0} \tag{34}$$

The system of equations proposed for the plasticity model (Eqs. (30)-(32)) needs also to be modified to include the deformational contribution of the sets of active smeared cracks ($\Delta\underline{\varepsilon}^{cr}$). By considering $\overline{\underline{\sigma}}_{n+1} = \overline{\underline{\sigma}}_{n} + \Delta\overline{\underline{\sigma}}_{n+1}$ and introducing Eqs. (2) and (23) into Eq. (18), yields after some arrangements in:

$$\left(\overline{\underline{\sigma}}_{n+1} - \left[\overline{\underline{\sigma}}_{n} + \underline{D}^{e}\left(\Delta\underline{\varepsilon}_{n+1} - \left[\underline{T}_{n+1}^{cr}\right]^{T}\Delta\underline{\varepsilon}_{\ell,n+1}^{cr}\right)\right]\right) + \Delta\lambda_{n+1}\underline{D}^{e}\left(\frac{\partial f}{\partial\overline{\underline{\sigma}}}\right)_{n+1} = \underline{0} \tag{35}$$

The equations describing the yield function (Eq. (31)) and the evolution law for hardening variable (Eq. (32)), still hold in the form deduced in section 2.2.3.2, since these equations are not affected by $\Delta\underline{\varepsilon}^{cr}$. To solve the system of nonlinear Eqs. (31), (32), (34) and (35) an iterative process was implemented to obtain the unknown variables, namely, the effective stress vector, $\overline{\underline{\sigma}}_{n+1}$, he incremental local crack strain vector, $\Delta\underline{\varepsilon}_{\ell,n+1}^{cr}$, the plastic multiplier, $\Delta\lambda_{n+1}$, and the hardening parameter, $\tilde{\epsilon}_{c,n+1}$, all of them at the *n+1* loading increment. This iterative process is similar to the return-mapping algorithm indicated in 2.2.3.2, whose details can be found elsewhere [34].

2.2.5 – Isotropic damage law

The stress vector ($\overline{\underline{\sigma}}_{n+1}$) obtained by solving the system of equations presented in the sections 2.2.3.2 and 2.2.4 is in the effective stress space, and must be transferred to the nominal stress space ($\underline{\sigma}_{n+1}$). For the damage models based on the isotropic damage mechanics, the evaluation of the nominal stress is performed by a damage-corrector step (Eq. 17) without an iterative calculation process. The present model adopts a damage-corrector process according to the Eq. (20), which considers the compressive damage scalar (d_c) only for negative (compressive) part of effective stress vector. The evaluation of the compressive damage scalar (d_c) during loading history is obtained according to the approach proposed by Gernay et al. [11]:

$$d_c(\tilde{\epsilon}_d) = 1 - \exp(-a_c \tilde{\epsilon}_d) \tag{36}$$

where $\tilde{\epsilon}_d$ is a scalar parameter known as damage internal variable.

Accordingly, the damage internal variable, $\tilde{\epsilon}_d$, can be evaluated as a function of the plasticity hardening variable, $\tilde{\epsilon}_c$, which is available at the end of plasticity analysis. As indicated in section 2.2.3.1, damage initiates at the plastic deformation corresponding to $\tilde{\epsilon}_{c1}$, then the damage internal variable, $\tilde{\epsilon}_d$, can be defined as:

$$\tilde{\epsilon}_d = \begin{cases} 0 & if\ \tilde{\epsilon}_c \le \tilde{\epsilon}_{c1} \\ \tilde{\epsilon}_c - \tilde{\epsilon}_{c1} & if\ \tilde{\epsilon}_c > \tilde{\epsilon}_{c1} \end{cases} \tag{37}$$

The non-dimensional parameter a_c indicates the degree of softening, and is obtained from [34]:

$$a_c = -\ln\left(\frac{0.05 f_c}{\bar{\sigma}_c(\tilde{\epsilon}_{cu})}\right) / (\tilde{\epsilon}_{cu} - \tilde{\epsilon}_{c1}) \tag{38}$$

being $\tilde{\epsilon}_{cu}$ the maximum equivalent strain in compression that is related to the compressive fracture energy, $G_{f,c}$, the characteristic length for compression, l_c, the compressive strength, f_c, and $\tilde{\epsilon}_{c1}$ according to the following equation [34]:

$$\tilde{\epsilon}_{cu} = \frac{3.1\, G_{f,c}}{l_c f_c} - \frac{11}{48}\tilde{\epsilon}_{c1} \tag{39}$$

and $\bar{\sigma}_c(\tilde{\epsilon}_{cu})$ is the hardening function evaluated at the maximum equivalent strain $\tilde{\epsilon}_{cu}$, see Fig. 5a.

Eq. (39) is a modified version of the equation originally proposed by Feenstra [35] for taking to account the exponential softening rate of compressive stresses (Eq. (36)). The compressive fracture energy, $G_{f,c}$, is assumed as the material parameter which can be derived based on experimental uniaxial stress-strain data; let's designate this experimental data as $\sigma_c - \varepsilon_c$. Similar to Eq. (26), the hardening parameter ($\tilde{\epsilon}_c$) corresponding to a generic axial strain (ε_c) is calculated as:

$$\tilde{\epsilon}_c = \varepsilon_c - \sigma_c / E \tag{40}$$

Then $G_{f,c}$ can be approximated as the area under post peak branch of $\sigma_c - \tilde{\epsilon}_c$ diagram [35] (see Fig. 6c). The characteristic lengths in tension (crack bandwidth) and compression (l_c) are usually considered the same [11, 35], then in the present approach $l_c = l_b$ was assumed.

3. PREDICTIVE PERFORMANCE OF THE MODEL

3.1 Introduction

In this section, the performance of the proposed model is assessed. For this purpose, PDSC constitutive model, described in section 2.2, was implemented into FEMIX 4.0 computer program [24] as a new approach to simulate the

nonlinear behaviour of cement based structures. FEMIX 4.0 is a computer code whose purpose is the analysis of structures by the Finite Element Method (FEM). This code is based on the displacement method, being a large library of types of finite elements available, namely 3D frames and trusses, plane stress elements, flat or curved elements for shells, and 3D solid elements. Linear elements may have two or three nodes, plane stress and shell elements may be 4, 8 or 9-noded and 8 or 20 noded hexahedra may be used in 3D solid analyses. This element library is complemented with a set of point, line and surface springs that model elastic contact with the supports, and also several types of interface elements to model inter-element contact. Embedded line elements can be added to other types of elements to model reinforcement bars. All these types of elements can be simultaneously included in the same analysis, with the exception of some incompatible combinations. The analysis may be static or dynamic and the material behaviour may be linear or nonlinear. Data input is facilitated by the possibility of importing CAD models. Post processing is performed with a general purpose scientific visualization program named *drawmesh*, or more recently by using GID.

In the same nonlinear analysis several nonlinear models may be simultaneously considered, allowing, for instance, the combination of reinforced concrete with strengthening components, which exhibit distinct nonlinear constitutive laws. Interface elements with appropriate friction laws and nonlinear springs may also be simultaneously considered. The global response history is recorded in all the sampling points for selected post-processing.

Advanced numerical techniques are available, such as the Newton-Raphson method combined with arc-length techniques and path dependent or independent algorithms. When the size of the systems of linear equations is very large, a preconditioned conjugate gradient method can be advantageously used.

The predictive performance of the proposed model (PDSC model) starts by executing numerical tests at the material level, and then at the structural level by simulating shear RC wall panel tests, and shear strengthened RC beams. The simulated structural elements are governed by nonlinear phenomenon due to simultaneous occurrence of cracking and inelastic deformation in compression.

3.2 Simulations at the material level

The stress-strain histories at the material (single element with one IP), loaded on some different scenarios are simulated by the proposed model (PDSC model). The loading procedure of the tests consists of imposing prescribed displacement increments and the crack bandwidth (l_b) was assumed equal to 100 mm. Since the concrete properties in each test were different, the corresponding values are indicated in the caption of the figures.

- *Monotonic and cyclic uniaxial compressive tests (Fig. 7 and 8):* A monotonic uniaxial compressive test of Kupfer et al. [36], and a cyclic uniaxial compressive test of Karsan and Jirsa [37] are simulated, and the predictive performance of the proposed model is appraised by comparing the numerical and experimental

results. Fig. 7 shows that the hardening and softening stress-strain branches registered experimentally by Kupfer et al. [36] are properly fitted by the nominal response of the proposed model. For comparison, Fig. 7 also represents the response of the model in effective stress space. As can be seen the stress-strain response in both effective and nominal stress spaces are identical for the domain before attaining the peak ($\tilde{\epsilon}_c \leq \tilde{\epsilon}_{c1}$), whereas for higher deformations ($\tilde{\epsilon}_c > \tilde{\epsilon}_{c1}$) the two responses starts diverging because of the damage initiation process ($d_c > 0$). Under the cyclic uniaxial compression the model (nominal stress response) accurately simulate the stress-strain envelope response registered experimentally, but overestimates the plastic deformation of the material when unloading occurs (Fig. 8), since the assumption of a constant predefined hardening inclination in Eq. (28) is a simplified approach to reduce the number of parameters required in the plasticity model. A more elaborated version of Eq. (28) is represented in Annex B which gives better approximation in simulation of the unloading phase. Another alternative to better predict the residual strain in unloading phases is to follow a more sophisticated diagram, like the one proposed by Barros et al. [38] but this approach it too demanding in terms of computer time consuming when integrated in a PDSC model, and when the final goal is using this model for the analysis of structures of relatively large dimensions.

- *Simulation of closing a crack developed in one direction, by imposing compressive load in the orthogonal direction (Fig. 9):* The element is initially subjected to the uniaxial tension in the direction of X_1 (Step 1). Then a crack is formed with the orientation of $\theta = 0^o$, and further propagated up to a stage that the crack does not be able to transfer more tensile stresses (fully opened crack status). At this stage the displacement in the direction of X_1 is fixed (Step 2), and the element is loaded by compressive displacements in the X_2 direction up to end of the analysis (Step 3).

  Due to applied compressive displacements, uniaxial compressive stresses are induced in the material in the X_2 direction. Consequently, expansion of the material in the X_1 direction imposes the crack be gradually closing. When the material is in the compression softening phase, in X_2 direction, the crack will be completely closed. When the crack closes, the state of stress is changed to biaxial compression, and a second hardening-softening response is reproduced corresponding to the appropriate biaxial state of stress. The above-described loading path was successfully simulated by the proposed model, and the prediction agrees well with the solution of Cervenka and Papanikolaou [16].

3.3 Simulations at the structural level

3.3.1 Shear RC walls

To highlight the efficiency of the proposed constitutive model, the two shear walls S1 and S4, tested by Maier and Thürlimann [39], were simulated. The experimental loading procedure introduces an initial vertical compressive force, F_v, and then a horizontal force, F_h, that was increased up to the failure of the wall. These shear walls had a relatively thick beam at their bottom and top edges for fixing the walls to the foundation, and for applying F_h and F_v, respectively, as depicted in Fig. 10a and 11a.

The walls, S1 and S4, differ in geometry, reinforcement ratio, and initial vertical load:

S4 - this wall has 1.18 *m* length, 1.2 *m* height, and 0.1 *m* thickness. It is reinforced in two layers of ϕ8 steel bars in both vertical and horizontal directions with the ratios of ρ_x = 1.03% and ρ_y = 1.05%, respectively. The initial vertical load is equal to $F_v = 262\,(kN)$, and more details on geometry, supports and loading configurations are presented at Fig. 10a.

S1 – the geometry of the wall S1 differs from that of the wall S4 due to the inclusion of vertical flanges at its lateral edges, see Fig. 11a. Theses flanges are reinforced vertically with the ratio of ρ_F = 1.16%, whereas the web reinforcements are ρ_x=1.03% and ρ_y = 1.16%. Moreover, an initial compressive load of $F_v = 433(kN)$ was applied, which is almost 1.65 times of the vertical load applied to the wall S4.

FEM modelling of the walls and top beams were performed using 8-noded serendipity plane stress finite elements with 3×3 Gauss-Legendre IP scheme, see Fig. 10b and Fig. 11b. Instead of modelling the foundation, the bottom nodes of the panels are fixed in vertical and horizontal directions. The vertical and horizontal loads are uniformly distributed over the edges of the top beam, as schematically represented in Fig. 10b and Fig. 11b. Elements of the top beam are assumed to exhibit linear elastic behaviour during the analysis, since no damage is reported for these elements in the original papers. For modelling the behaviour of the steel bars, the stress-strain relationship represented in Fig. 12 was adopted. The curve (under compressive or tensile loading) is defined by the points PT1 = ($\varepsilon_{sy}, \sigma_{sy}$), PT2 = ($\varepsilon_{sh}, \sigma_{sh}$), and PT3 = ($\varepsilon_{su}, \sigma_{su}$) and a parameter P that defines the shape of the last branch of the curve. Unloading and reloading linear branches with the slop of $E_{sy} = \sigma_{sy} / \varepsilon_{sy}$ are assumed in the present approach [22].

The reinforcement is meshed using 2-noded perfect bonded embedded cables with two IPs. The values of parameters used to define the constitutive models of concrete and steel are included in Table 1 and Table 2, respectively. The effect of tension-stiffening was indirectly simulated using the trilinear tension-softening diagram.

The experimental relationship between the applied horizontal force and the the horizontal displacement of the top beam, F_h-U_h, for the wall S4 is represented in Fig. 10c. This figure also includes the predicted F_h-U_h response obtained by both PDSC and SC models. According to the experimental observations, the wall S4 exhibits a ductile F_h-U_h response after attaining the peak load, and the failure was governed by crushing of concrete at the bottom left side of the panel. Predictions of the PDSC model are obtained for three levels of compressive fracture energy ($G_{f,c} = 20, 30, 40\, N/mm$)

to evident the effect of different rate of compressive softening on behaviour of the simulated wall. At $U_h \approx 4\,mm$ the IP closest to the left bottom side of the wall enters to the compressive softening phase ($d_c > 0$). After $U_h \approx 7\,mm$ the load carrying capacity and ductility of the simulated F_h-U_h responses are significantly affected by changing the compressive fracture energy; the load carrying capacity and ductility increase with $G_{f,c}$. Ductility of the wall is underestimated for the simulation with $G_{f,c} = 20\,N/mm$, and overestimated when using $G_{f,c} = 40\,N/mm$. A proper fit of the experimentally observed ductility and softening response after peak load was obtained for $G_{f,c} = 30\,N/mm$. This value is close to the upper limit of the interval values obtained by Vonk [40]. Fig. 10e and Fig. 10f present, respectively, the numerical crack pattern and the plastic zone, i.e. the area indicating those IPs under inelastic compressive deformation ($\tilde{\epsilon}_c > 0$), for the simulation using $G_{f,c} = 30\,N/mm$, at the deformation corresponding to $U_h \approx 18\,mm$ (final converged step). A general analysis of Fig. 10e and Fig. 10f demonstrate the cracks with fully opened status are spread over the right lower side of the panel (tensile zone) while the plastic zones are concentrated at the bottom left corner of the panel. This numerical prediction correlates well with the experimental observations (see Fig. 10d).

The F_h-U_h prediction of the SC model is similar to those of the PDSC model only in the beginning stage (up to $U_h \approx 1\,mm$) when inelastic deformation due to compression is negligible, but for higher displacements the two models start diverging significantly. The SC model does not consider the inelastic behaviour of concrete under compression that justifies the significant overestimation of the predicted load carrying capacity of the simulated panel.

Results of the analysis of the wall S1 are represented in Fig. 11 in terms of F_h-U_h relationship, crack pattern, and plastic zone. As can be seen in Fig. 11c the PDSC model assuming $G_{f,c} = 30\,N/mm$ was able to accurately predict the overall experimental F_h-U_h behaviour of this wall. The simulated plastic zone clearly evidence the formation of a larger compressive strut when compared to what happened in the wall S4, which is due to the higher initial vertical load and the confinement provided by the additional vertical flanges.

3.3.2 Shear strengthened RC beams

3.3.2.1 Beam prototypes

The experimental program [41] is composed of a reference beam (Fig. 13) and four NSM shear strengthened beams (Fig. 14). Fig. 13 represents the T cross section geometry and the steel reinforcement detailing for the series of beams, as well as the loading configuration and support conditions. The adopted reinforcement systems were designed to assure shear failure mode for all the tested beams. To localize the shear failure in only the monitored shear spans, a_{sp}, a three point loading configuration with a distinct length for the beam shear spans was selected, as shown in Fig. 13. Steel

stirrups of 6 mm diameter at a spacing of 112 mm (ϕ6@112mm) were applied in the b_{sp} beam span to avoid shear failure.

The differences between the tested beams are restricted to the shear reinforcement systems applied in the a_{sp} beam span. The reference beam is designated as 3S-R (three steel stirrups in the a_{sp} shear span, 3S, leading a steel shear reinforcing ratio, ρ_{sw}, of 0.09%), while the following different NSM strengthening configurations were adopted for the other four beams that also include 3 steel stirrups in the a_{sp} shear span (Fig. 14 and Tables 3 and 4):

3S-4LI-S2 - four CFRP laminates of type 2 (with a cross section of 1.4×20 mm^2) per face, inclined at 52 degrees with respect to the longitudinal axis of the beam (θ_f = 52º), and installed from the bottom surface of the flange to the bottom tensile surface of the beam's web, i.e., bridging the total lateral surfaces of the beam's web; each CFRP laminate was installed in the outer part of a slit of a depth of 21 mm executed on the beam's web lateral surfaces. The length of each laminate was 634 mm;

3S-4LI-P2 - four CFRP laminates of type 2 (with a cross section of 1.4×20 mm^2) per face, inclined at 52 degrees with respect to the longitudinal axis of the beam (θ_f = 52º), and installed from the bottom surface of the flange up to 10 mm above the top surface of the longitudinal tensile steel reinforcement. Each CFRP laminate was installed in the deeper part of a slit of a depth of 35 mm from the surface of the beam's web lateral surfaces. The length of each laminate was 527 mm;

3S-4LI4LI-SP1 - eight CFRP laminates of type 1 (with a cross section of 1.4×10 mm^2) per face, inclined at 52 degrees with respect to the longitudinal axis of the beam (θ_f = 52º). The configuration of the slits executed in this section combines the configurations of the beams 3S-4LI-P2 and 3S-4LI-S2. In each slit, with a depth of 35mm, was installed one laminate as deeper as possible and one laminate as superficial as possible.

3S-4LI4LV-SP1 - eight CFRP laminates of type 1 (with a cross section of 1.4×10 mm^2) per face, four of them inclined at 52 degrees with respect to the longitudinal axis of the beam (θ_f = 52º) and bridging the total lateral surfaces of the beam's web (the length of each inclined laminate was 634 mm), while the other four laminates were installed in vertical slits executed from the bottom surface of the web up to 10 mm above the top surface of the longitudinal tensile steel reinforcement (the length of each vertical laminate was 432 mm). The vertical laminates were installed as deeper as possible into a slit of a depth of 35 mm from the surface of the beam's web lateral surfaces. The inclined laminates were installed as outer as possible into a slit of a depth of 15 mm executed on the beam's web lateral surfaces.

The details of the shear strengthening configurations are indicated in Table 3, where it is verified that the tested beams had a percentage of longitudinal tensile steel bars (ρ_{sl}) of 2%, a percentage of steel stirrups (ρ_{sw}) of 0.09%, and a percentage of NSM CFRP laminates ranging from 0.101% to 0.113%.

3.3.2.2 Material properties

All the NSM shear strengthened beams were executed with a concrete that presented an average compressive strength (f_c) of 40.1 MPa. For the reference beam 3S-R the value of f_c was 36.4 MPa. The average value of the yield stress of the steel bars of 6, 12, 16 and 32 mm diameter was 556.1, 566.6, 560.8 and 654.5 MPa, respectively, while average value of the ultimate stress for these corresponding bars was: 682.6, 661.6, 675.0 and 781.9 MPa. The constitutive law for the steel bars follows the stress-strain relationship represented in Fig. 12, and values for its definition are those indicated in Table 5. The CFRP laminates presented a linear-elastic stress-strain response with a tensile strength of 3009 MPa and an elasticity modulus of 169 GPa and 166 GPa for the laminate type 1 and 2, respectively. The complementary discussion on the characterization of the CFRP laminates and epoxy adhesive can be found in Barros and Dias [41].

3.3.2.3 Finite element modelling and constitutive laws for the materials

The finite element mesh of 8-noded plain stress finite element with 2×2 Gauss-Legendre IP scheme, represented in Fig. 15, was adopted (corresponds to the 3S-4LI-S2 beam, but the differences for the other beams are limited to the CFRP strengthening configurations). To avoid local crushing of the concrete, the load and support conditions were applied through steel plates that are modeled as a linear-elastic material with Poisson's coefficient of 0.3 and elasticity modulus of 200 *GPa*. The longitudinal steel bars, stirrups and CFRP laminates were modelled using 2-noded embedded cables (one degree-of-freedom per each node) with two IPs. Perfect bond was assumed between the reinforcement and the surrounding concrete. The behaviour of CFRP laminates was modeled using a linear-elastic stress-strain relationship.

The values correspondent to the parameters of the constitutive model for concrete is gathered in Table 6. These values are obtained from the experimental program for the characterization of the relevant properties of the intervening materials. For the $G_{f,c}$ the average value of the interval proposed by Vonk [40] was assumed.

To simulate the shear crack initiation and the degradation of crack shear stress transfer, the shear softening diagram represented in Fig. 2 is assumed, and the values of the parameters to define this diagram are included in Table 6. Due to lack of reliable experimental evidences to characterize this diagram, the adopted values are indirectly obtained from the test data using the inverse method (by simulating the experimental results as best as possible) [23]. In general by increasing $G_{f,s}$ and $\tau_{t,p}^{cr}$, and decreasing β, the load carrying capacity of RC elements failing in shear increases. To define reliable intervals of values for these parameters, a comprehensive parametric study is necessary to be executed, which is planned to be executed in next future by the authors. Based on the experience of the authors, however, the following intervals of values can be recommended for RC beams with regular shear and flexural reinforcement ratios: $\tau_{t,p}^{cr} \in [1.0-3.0]$ MPa; $G_{f,s} \in [0.04-0.5]$ N/mm; $\beta \in [0.02-0.3]$.

3.3.2.4 Results and discussions

For the shear strengthened beams (3S-4LI-S2; 3S-4LI-P2; 3S-4LI4LI-SP1; 3S-4LI4LV-SP1), the transversal reinforcement (CFRP laminates and steel stirrups) provides additional confinement effect on the surrounding concrete bulk. This confinement enhances the aggregate interlock effect in the shear cracks crossed by these shear reinforcements. For these beams, even though the CFRP laminates and steel stirrups are separately modelled with embedded cable elements, their favourable effect in terms of aggregate interlock was considered by adopting different values of shear fracture energy ($G_{f,s}$) for the reference and strengthened beams. Since the equivalent shear reinforcement ratio (CFRP laminates and steel stirrups) was not too different amongst the strengthened beams, the same value of $G_{f,s} = 0.3\ N/mm$ was adopted in the constitutive model, while in the reference beam a $G_{f,s} = 0.04\ N/mm$ was assumed, see Table 6. In fact, by increasing $G_{f,s}$ the beam's stiffness and load carrying capacity also increase, which indirectly simulates the favorable effect of the shear reinforcements on the aggregate interlock.

Predictions of the PDSC model in terms of the applied load versus the displacement at the loaded section for all the beams of the experimental program are represented at Fig. 16. The good predictive performance was not only in terms of the load-deformation responses, but also in regards of the crack patterns (Figs. 17 and 18). The plastic zone for each beam is also represented in Fig. 18 that demonstrate the formation of the compressive strut in this type of shear tests.

4. CONCLUSIONS

In the present study, a constitutive law for cement based materials is proposed that combines a multi-directional fixed smeared crack model to account for cracking, and a plasticity-damage model to simulate the inelastic compressive behaviour of materials between the cracks. The crack opening process is initiated based on the Rankine tensile criterion, whereas a trilinear softening diagram is used to simulate the crack propagation. Two methods are available to simulate the crack shear stress transfer: one based on the concept of shear retention factor (β), and the other on a shear softening diagram that requires some information about fracture mode II propagation. The plasticity model is formulated in effective (undamaged) stress space and adopts a single hardening parameter to account for the compressive plastic deformations. The plasticity approach is combined with an isotropic damage model to account for strength and stiffness degradation of the material under compression. An algorithm is, also, proposed that accounts for simultaneous occurrence of cracking in tension and inelastic compressive deformation of material between the cracks.

The constitutive model was implemented in the finite element computer code FEMIX, and its performance was assessed by simulating experimental tests at material and structural levels. The potentialities of the proposed model for simulating RC elements governed simultaneously by cracking and inelastic deformation in compression were investigated by simulating shear wall panel tests, and an experimental program composed by T cross section RC beams

shear strengthened with different configurations of NSM-CFRP laminates. The results of these analyses demonstrate the applicability of the proposed model for simulating structures made by cement based materials subjected to multi-axial loading configurations.

ACKNOWLEDGEMENTS

The authors wish to acknowledge the FCT financial support provided by the Portuguese Foundation for Science and Technology in the scope of the SlabSys-HFRC research project, with reference PTDC/ECM/120394/2010.

ANNEX A

According to the Willam-Warnke failure criterion, two extreme meridians and an elliptical function, used to interpolate the current failure meridian between the two extreme meridians, can represent the entire failure surface. The extreme meridians are called the tensile meridian where angle of similarity is zero $(\theta = 0^\circ)$, and the compressive meridian where $\theta = 60^\circ$ (see Fig. A.1).

The equations for the tensile and compressive meridians in $(\bar{\xi}, \bar{\rho}, \bar{\theta})$ coordinate system are given by the following quadratic parabolas [29]:

$$\frac{\bar{\xi}}{f_c} = a_2\left(\frac{\bar{\rho}_{(\bar{\xi},\bar{\theta}=0^\circ)}}{f_c}\right)^2 + a_1\left(\frac{\bar{\rho}_{(\bar{\xi},\bar{\theta}=0^\circ)}}{f_c}\right) + a_0 \quad \text{(A.1)}$$

$$\frac{\bar{\xi}}{f_c} = b_2\left(\frac{\bar{\rho}_{(\bar{\xi},\bar{\theta}=60^\circ)}}{f_c}\right)^2 + b_1\left(\frac{\bar{\rho}_{(\bar{\xi},\bar{\theta}=60^\circ)}}{f_c}\right) + b_0 \quad \text{(A.2)}$$

being $\bar{\xi}$ the hydrostatic stress invariant defined as $\bar{\xi} = \bar{I}_1/3$, and $\bar{\rho}$ the deviatoric stress invariants also defined as $\bar{\rho} = \sqrt{2\bar{J}_2}$. The term $\bar{\rho}_{(\bar{\xi},\bar{\theta})}$ implies the deviatoric stress invariant ($\bar{\rho}$) that is corresponds to any set of $\bar{\xi}$ and $\bar{\theta}$. For the tensile meridian (where $\theta = 0^\circ$) and compressive meridian (where $\theta = 60^\circ$), the deviatoric stress invariant **(** $\bar{\rho}$ **)** are denoted, respectively, by $\bar{\rho}_{(\bar{\xi},\bar{\theta}=0^\circ)}$ and $\bar{\rho}_{(\bar{\xi},\bar{\theta}=60^\circ)}$.

It is assumed that the tensile and compressive parabolas (meridians) intersect each other at the hydrostatic axis, $\bar{\rho} = \sqrt{2\bar{J}_2} = 0$, therefore $a_0 = b_0$ [29]. The constants a_0, a_1, a_2, b_1 and b_2 are the five constants of the W-W failure surface, and they are defined in **(** $\bar{\xi}$, $\bar{\rho}$, $\bar{\theta}$ **)** coordinate system such that [34]:

$$a_0 = \frac{\sqrt{3}(7.4241\mu + 0.6737\mu^2)}{8.197 - 9.0605\mu + 1.6814\mu^2} \quad \text{(A.3a)}$$

$$a_1 = \frac{\sqrt{3}(-5.7392 - 3.694\mu - 2.091\mu^2)}{8.197 - 9.0605\mu + 1.6814\mu^2} \tag{A.3b}$$

583

$$a_2 = \frac{\sqrt{3}(-1.0098 + 3.3911\mu)}{8.197 - 9.0605\mu + 1.6814\mu^2} \tag{A.3c}$$

584

$$b_1 = \frac{\sqrt{3}(-2.3328 - 9.169\mu - 1.5469\mu^2)}{8.197 - 9.0605\mu + 1.6814\mu^2} \tag{A.3d}$$

585

$$b_2 = \frac{\sqrt{3}(-1.2437 + 4.6489\mu + 0.004254\mu^2)}{8.197 - 9.0605\mu + 1.6814\mu^2} \tag{A.3e}$$

586

587 being μ a non-dimensional parameter defined as $\mu = f_{ct}/f_c$. The details corresponding to the Eq. (A.3) are available
588 elsewhere [34].

589 The W-W failure criterion uses the following elliptical equation to interpolate current failure meridian, or the
590 intermediate failure meridians, between the two extremes (tensile and compressive meridians) [17, 29]:

$$\bar{\rho}_{(\bar{\xi},\bar{\theta})} = \frac{s}{t} \tag{A.4a}$$

591 where

$$\begin{aligned} s = {} & 2\bar{\rho}_{(\bar{\xi},\bar{\theta}=60^\circ)}(\bar{\rho}^2_{(\bar{\xi},\bar{\theta}=60^\circ)} - \bar{\rho}^2_{(\bar{\xi},\bar{\theta}=0^\circ)})\cos\bar{\theta} + \bar{\rho}_{(\bar{\xi},\bar{\theta}=60^\circ)}(2\bar{\rho}_{(\bar{\xi},\bar{\theta}=0^\circ)} - \bar{\rho}_{(\bar{\xi},\bar{\theta}=60^\circ)}) \\ & \times\left[4(\bar{\rho}^2_{(\bar{\xi},\bar{\theta}=60^\circ)} - \bar{\rho}^2_{(\bar{\xi},\bar{\theta}=0^\circ)})\cos^2\bar{\theta} + 5\bar{\rho}^2_{(\bar{\xi},\bar{\theta}=0^\circ)} - 4\bar{\rho}_{(\bar{\xi},\bar{\theta}=0^\circ)}\bar{\rho}_{(\bar{\xi},\bar{\theta}=60^\circ)}\right]^{1/2} \end{aligned} \tag{A.4b}$$

592 and

$$t = 4(\bar{\rho}^2_{(\bar{\xi},\bar{\theta}=60^\circ)} - \bar{\rho}^2_{(\bar{\xi},\bar{\theta}=0^\circ)})\cos^2\bar{\theta} + (\bar{\rho}_{(\bar{\xi},\bar{\theta}=60^\circ)} - 2\bar{\rho}_{(\bar{\xi},\bar{\theta}=0^\circ)})^2 \tag{A.4c}$$

593 being $\bar{\rho}_{(\bar{\xi},\bar{\theta})}$ is the deviatoric stress invariant of current failure meridian (see Fig. A.1b that demonstrates the deviatoric
594 plane of W-W). As Fig. A.1b shows, Eq. (A.4) ensures convexity and smoothness of the surface anywhere. Eqs. (A.1),
595 (A.2) and (A.4) describe one sixth of the failure cone lying between $0 \le \bar{\theta} \le 60$, then due to six fold symmetry, these
596 equations are sufficient to present the entire failure surface.

597 The intermediate failure meridians are also quadratic parabola in a form [29]:

$$\frac{\bar{\xi}}{f_c} = a\left(\frac{\bar{\rho}_{(\bar{\xi},\bar{\theta})}}{f_c}\right)^2 + b\left(\frac{\bar{\rho}_{(\bar{\xi},\bar{\theta})}}{f_c}\right) + c \tag{A.5}$$

598 The intermediate meridian must also meet the hydrostatic axis at the same location that tensile and compressive
599 meridians already intersected, such a requirement implies that:

$$c = a_0 = b_0 \tag{A.6}$$

The two unknowns a and b are determined by solving Eq. (A.5) in two known failure points laying on the intermediate failure meridian. Based on the current state of effective stress vector ($\underline{\bar{\sigma}}$) the angle of similarity is calculated from Eq. (22). The arbitrary control points of $\bar{\xi}/f_c = -2$ and $\bar{\xi}/f_c = -4$ were chosen [29], then the corresponding failure points of $\bar{\rho}_{(\bar{\xi}=-2,\,\bar{\theta})}$, and $\bar{\rho}_{(\bar{\xi}=-4,\,\bar{\theta})}$ were interpolated from Eq. (A.4). The coefficients a and b can then be obtained from [29]:

$$a = \frac{(-4.0 - a_0) - b\left(\dfrac{\bar{\rho}_{(\bar{\xi}=-4,\,\bar{\theta})}}{f_c}\right)}{\left(\dfrac{\bar{\rho}_{(\bar{\xi}=-4,\,\bar{\theta})}}{f_c}\right)^2} \tag{A.7}$$

$$b = \frac{(4.0 + a_0)\left(\dfrac{\bar{\rho}_{(\bar{\xi}=-2,\,\bar{\theta})}}{f_c}\right)^2 + (-2.0 - a_0)\left(\dfrac{\bar{\rho}_{(\bar{\xi}=-4,\,\bar{\theta})}}{f_c}\right)^2}{\left(\dfrac{\bar{\rho}_{(\bar{\xi}=-4,\,\bar{\theta})}}{f_c}\right)\left[\left(\dfrac{\bar{\rho}_{(\bar{\xi}=-2,\,\bar{\theta})}}{f_c}\right)\left(\dfrac{\bar{\rho}_{(\bar{\xi}=-4,\,\bar{\theta})}}{f_c}\right) - \left(\dfrac{\bar{\rho}_{(\bar{\xi}=-2,\,\bar{\theta})}}{f_c}\right)^2\right]} \tag{A.8}$$

Including $\bar{\xi} = \bar{I}_1/3$ and $\bar{\rho}_{(\bar{\xi},\,\bar{\theta})} = \sqrt{2\bar{J}_2}$ into Eq. A.5 and replacing f_c with the current uniaxial compressive stress, i.e. the hardening function denoted by $\bar{\sigma}_c$, the equation of yield function is obtained in the form of Eq. (21).

ANNEX B

The $\bar{\sigma}_c - \tilde{\epsilon}_c$ law for the domain $\tilde{\epsilon}_c > \tilde{\epsilon}_{c1}$ (Eq. (28)) can be modified to include the parameter κ that controls the slop of this branch such that:

$$\bar{\sigma}_c(\tilde{\epsilon}_c) = \frac{f_c}{\kappa - \tilde{\epsilon}_{c1}}(\tilde{\epsilon}_c - \tilde{\epsilon}_{c1}) + f_c \tag{B.1}$$

where κ is calculated as $\kappa = l_0\,\tilde{\epsilon}_{c1}$, and the non-dimensional coefficient l_0 can take the values as $1 < l_0 < \infty$. For $l_0 = \infty$ Eq. (B.1) gives $\bar{\sigma}_c(\tilde{\epsilon}_c) = f_c$ that corresponds to ideal plastic behaviour (slop of $\bar{\sigma}_c - \tilde{\epsilon}_c$ law for the domain $\tilde{\epsilon}_c > \tilde{\epsilon}_{c1}$ becomes zero). Using the values of the parameters of the constitutive model in the simulation of cyclic test of Karsan and Jirsa [37], Fig. B.1a represents the Eq. (28), and Eq. (B.1) for two distinct values of $l_0 = 4.5$ and $l_0 = 9.0$. As can be seen in this figure, by increasing the value of l_0 the inclination of the $\bar{\sigma}_c - \tilde{\epsilon}_c$ law is decreased. The appropriate value for the parameter l_0 is usually obtained using an inverse analysis whereas such inverse method is described in the contribution Abu Al-Rub and Kim [14]. For the case $l_0 = 4.5$ (assuming all the other parameters have

618 the same values as described in Fig. 7) the cyclic stress strain response of the model for the test of Karsan and Jirsa [37]
619 is represented in Fig. B.1b which demonstrates a close approximation of the residual plastic deformations in compare to
620 those registered as the experimental.

621

622 **REFERENCES**

623 [1] Hillerborg, A., Modéer, M. and Petersson, P. E., "Analysis of crack formation and crack growth in concrete by
624 means of fracture mechanics and finite elements", Cement and Concrete Research, 6(6): 773-781, 1976.
625 [2] Bažant, Z. P. and Oh, B. H., "Crack band theory for fracture of concrete", Materials and Structures, 16(3): 155-177,
626 1983.
627 [3] Moës, N. and Belytschko, T., "Extended finite element method for cohesive crack growth", Engineering Fracture
628 Mechanics, 69(7): 813-833, 2002.
629 [4] Lubliner, J., Oliver, J., Oller, S. and Oñate, E., "A plastic-damage model for concrete", International Journal of
630 Solids and Structures, 25(3): 299-326, 1989.
631 [5] De Borst, R. and Muehlhaus, H. B., "Gradient-dependent plasticity: Formulation and algorithmic aspects",
632 International Journal for Numerical Methods in Engineering, 35(3): 521-539, 1992.
633 [6] de Borst, R., "Computational aspects of smeared crack analysis", In: Hinton, E., Owen, D.R.J. (Eds.),
634 Computational Modelling of Reinforced Concrete. Pineridge Press, Swansea, pp. 44–83, 1986.
635 [7] Mazars, J. and Pijaudier-Cabot, G., "Continuum damage theory - application to concrete ", Journal of Engineering
636 Mechanics, 115(2): 345-365, 1989.
637 [8] Grassl, P. and Jirasek, M., "Damage–plastic model for concrete failure", International Journal of Solids and
638 Structures, 43:7166–7196, 2006.
639 [9] Wu, J.U., Li J. and Faria, R., "An energy release rate-based plastic-damage model for concrete", International
640 Journal of Solids and Structures, 43:583–612, 2006.
641 [10] Grassl, P., Xenos, D., Nystrom, U., Rempling, R. and Gylltoft, K., "CDPM2: A damage-plasticity approach to
642 modelling the failure of concrete", International Journal of Solids and Structures, 50:3805–3816, 2013.
643 [11] Gernay, T., Millard, A. and Franssen, J., "A multiaxial constitutive model for concrete in the fire situation:
644 Theoretical formulation", International Journal of Solids Structures, 50:3659-3673, 2013.
645 [12] Omidi, O. and Lotfi, V., "Continuum large cracking in a rate-dependent plastic–damage model for cyclic-loaded
646 concrete structures", International Journal for Numerical and Analytical Methods in Geomechanics, 37:1363–1390,
647 2013.

[13] Taqieddin, Z., Voyiadjis, G.Z. and Almasri, A.H., "Formulation and verification of a concrete model with strong coupling between isotropic damage and elastoplasticity and comparison to a weak coupling model", Journal of Engineering Mechanics ASCE, 138:530–541, 2012.

[14] Abu Al-Rub, R.K. and Kim, S.M., "Computational applications of a coupled plasticity–damage constitutive model for simulating plain concrete fracture", Engineering Fracture Mechanics, 77 (10):1577–1603, 2010.

[15] Lee, J. and Fenves, G.L., "Plastic-damage model for cyclic loading of concrete structures", Journal of Engineering Mechanics Division, ASCE, 124, 892–900, 1998.

[16] Cervenka, J. and Papanikolaou, V., "Three dimensional combined fracture–plastic material model for concrete", International Journal of Plasticity, 24:2192–2220, 2008.

[17] Willam, K. J. and Warnke, E.P., "Constitutive model for the triaxial behaviour of concrete in Concrete Structures Subjected to Triaxial Stresses.", volume 19 of IABSE Report, International Association of Bridge and Structural Engineers, Zurich, pp: 1-30, 1974.

[18] Menetrey, Ph. and Willam, K.J., "Triaxial failure criterion for concrete and its generalization", ACI Structural Journal, 92, 311–318, 1995.

[19] Grassl, P., Lundgren, K. and Gylltoft. K., "Concrete in compression: a plasticity theory with a novel hardening law", International Journal of Solids and Structures, Vol. 39, pp: 5205–5223, 2002.

[20] Pereira, E.B., "Processes of Cracking in Strain Hardening in Cementitious Composites", PhD Thesis, University of Minho, Portugal, 2012.

[21] Park, H. and Kim, J. Y., "Plasticity model using multiple failure criteria for concrete in compression", International Journal of Solids and Structures, 42(8), pp. 2303-2322, 2005.

[22] Sena-Cruz, J. M., "Strengthening of concrete structures with near-surface mounted CFRP laminate strips", PhD thesis, Department of Civil Engineering, University of Minho, 2004.

[23] Ventura-Gouveia, A., "Constitutive models for the material nonlinear analysis of concrete structures including time dependent effects", PhD thesis, Department of Civil Engineering, University of Minho, 2011.

[24] Sena-Cruz, J.M., Barros, J.A.O., Azevedo, A.F.M. and Ventura-Gouveia, A., "Numerical simulation of the nonlinear behaviour of RC beams strengthened with NSM CFRP strips", Proceedings of CMNE/CILAMCE Congress, FEUP, Porto, Portugal, June, 2007.

[25] De Borst, R. and Nauta, P., "Non-orthogonal cracks in a smeared finite element model", Engineering Computations, 2:35-46, 1985.

[26] Kachonov, L.M. On the creep fracture time. Izv. Akad. Nauk USSR Otd. Tech, 8:26–31, 1958 [in Russian].

[27] Shah S.P., Swartz S.E. and Ouyang C., "Fracture mechanics of concrete: applications of fracture mechanics to concrete, rock and other quasi-brittle materials", John Wiley & Sons, Inc; 1995.

680 [28] Ortiz, M., "A constitutive theory for inelastic behaviour of concrete", Mechanics of Materials, 4:67–93, 1985.
681 [29] Swaddiwudhipong, S. and Seow, P.E.C., "Modelling of steel fiber-reinforced concrete under multi-axial loads",
682 Cement and Concrete Research, 36, pp. 1354–1361, 2006.
683 [30] Dunne, F. and Petrinic, N., "Introduction to computational plasticity", Oxford University Press, 2005.
684 [31] Ristinmaa, M., Wallin, M. and Ottosen, N.S., "Termodynamic format and heat generation of isotropic hardening
685 plasticity", Acta Mechanica, April 2007 (published online).
686 [32] CEB-FIB, CEB-FIP Model Code 1990 - Design Code, Thomas Telford, (1993).
687 [33] Simo, J. C. and Hughes, T. J. R., "Computational inelasticity", Springer, 1998.
688 [34] Edalat Behbahani, A., Barros, J.A.O. and Ventura Gouveia, A., "Plastic-Damage Smeared cracking constitutive
689 modelling of cement based materials", Report No. DEC/E-22, University of Minho, 2015.
690 [35] Feenstra, P. H., "Computational aspect of biaxial stress in plain and reinforced concrete" PhD thesis, Department
691 of Civil Engineering, Delft University of Technology, 1993.
692 [36] Kupfer, H., Hilsdorf, H. K., and Rusch, H., "Behaviour of concrete under biaxial states of stress" Am Concrete
693 Institute journal, 66(8):656–66, 1969.
694 [37] Karsan, I.D., Jirsa, J.O., "Behaviour of concrete under compressive loadings" Journal of Structure Division, ASCE
695 95 (12), 2535– 2563, 1969.
696 [38] Barros, J.A.O., Varma, R.K., Sena-Cruz, J.M., Azevedo, A.F.M., "Near surface mounted CFRP strips for the
697 flexural strengthening of RC columns - experimental and numerical research", Engineering Structures Journal, 30(12),
698 3412-3425, December 2008.
699 [39] Maier, J. and Thürlimann, B., "Bruchversuche an Stahlbetonscheiben", IBK Bericht 8003-1, ETH Zürich, Institut
700 für Baustatik und Konstruktion (IBK), Zürich, 1985.
701 [40] Vonk, R.A., "Softening of concrete loaded in compression", PhD thesis, Eindhoven University of Technology, The
702 Netherlands, 1992.
703 [41] Barros, J. and Dias, S., "Assessment of the effectiveness of the NSM shear strengthening technique for deep T
704 cross section RC beams", FRPRCS11, Guimaraes, Portugal, 2013.
705
706
707
708
709
710

711

NOTATIONS

$\underline{\bar{\sigma}}$	stress vector at global coordinate system providing no compressive damage is included
$\underline{\sigma}$	stress vector at global coordinate system which include compressive damage softening
$\underline{D}^e$	linear elastic constitutive matrix
$\underline{\bar{\sigma}}^+$	the positive component, corresponding to tensile state of stress, of stress vector $\underline{\bar{\sigma}}$
$\underline{\bar{\sigma}}^-$	the negative component, corresponding to compressive state of stress, of stress vector $\underline{\bar{\sigma}}$
$\bar{\sigma}^i$	*i*th principle stress extracted from the vector $\underline{\bar{\sigma}}$
$\underline{P}^i$	the normalized eigenvector associated with the *i*th principle stress $\bar{\sigma}^i$
$\Delta\underline{\varepsilon}^{cr}$	incremental crack strain vector
$\Delta\underline{\varepsilon}^{co}$	incremental concrete strain vector
$\Delta\underline{\varepsilon}$	incremental total strain vector
$\Delta\underline{\varepsilon}^{p}$	incremental plastic strain vector
θ_i	orientation corresponding to the *i-th* crack
IP	integration point
$\Delta\underline{\varepsilon}_{\ell}^{cr}$	incremental crack strain vector at crack coordinate system
$\Delta\underline{\sigma}_{\ell}^{cr}$	incremental stress vector at crack coordinate system
σ_n^{cr}	normal components of the local crack stress vector
τ_t^{cr}	shear components of the local crack stress vector
ε_n^{cr}	normal components of the local crack strain vector
γ_t^{cr}	shear components of the local crack strain vector
$\underline{T}^{cr}$	transformation matrix from crack local coordinate system to finite element coordinate system
$\underline{D}^{cr}$	crack constitutive matrix
D_n^{cr}	the stiffness modulus correspondent to the fracture mode I
D_t^{cr}	the stiffness modulus correspondent to the fracture mode II
E	modulus of elasticity
ν	Poisson's coefficient

α_i	normalized stress parameters (i=1, 2) in trilinear diagram
β	shear retention factor
ξ_i	normalized strain parameter (i =1, 2) in trilinear diagram
f_c	compressive strength of concrete
f_{ct}	tensile strength of concrete
G_c	elastic shear modulus
G_f^I	mode I fracture energy
$G_{f,s}$	mode II fracture energy
$G_{f,c}$	compressive fracture energy
l_b	crack bandwidth
l_c	Compressive characteristic length which was assumed identical to the crack bandwidth
$\varepsilon_{n,u}^{cr}$	ultimate crack normal strain
P_1	parameter that defines the amount of the decrease of β upon increasing ε_n^{cr}
$\gamma_{t,p}^{cr}$	peak crack shear strain
$\tau_{t,p}^{cr}$	peak crack shear stress
$\gamma_{t,u}^{cr}$	ultimate crack shear strain
$\bar{I}_1$	first invariant of the effective stress tensor
$\bar{J}_2$	second invariant of the deviatoric effective stress tensor
$\bar{J}_3$	third invariant of deviatoric stresses
$\bar{\theta}$	angle of similarity
$\bar{\xi}$	hydrostatic stress invariant
$\bar{\rho}$	deviatoric stress invariants
a, b, c	parameters of Willam-Warnke yield surface depending to state of stress
$\bar{\sigma}_c$	hardening function of the plasticity model

ε_{c1}	strain at compression peak stress
$f(\bar{\underline{\sigma}}, \bar{\sigma}_c)$	yield function
$\tilde{\epsilon}_c$	compressive hardening variable
$\Delta\lambda$	plastic multiplier
$\tilde{\epsilon}_{c1}$	accumulated plastic strain at uniaxial compressive peak stress
f_{c0}	uniaxial compressive stress at plastic threshold
α_0	material constant to define the beginning of the nonlinear behaviour in uniaxial compressive stress-strain test
d_c	scalar describing the amount compressive damage
$\tilde{\epsilon}_d$	internal damage variable for compression
a_c	non-dimensional parameter of damage
ρ_x	horizontal reinforcement ratio of web of the shear wall panel
ρ_y	vertical reinforcement ratio of web of the shear wall panel
ρ_F	reinforcement ratio corresponding to the vertical flange of the shear wall panel
F_v	initial vertical load applied to the shear wall panel
F_h	horizontal load applied to the shear wall panel
$\varepsilon_{sy}, \varepsilon_{sh}, \varepsilon_{su}$	three strain points at the steel constitutive law
$\sigma_{sy}, \sigma_{sh}, \sigma_{su}$	three stress points at the steel constitutive law
P	parameter that defines the shape of the last branch of the steel stress-strain curve
E_{sy}	unloading-reloading slop for the steel constitutive law
U_h	horizontal deformation of the panel
a_{sp}	monitored span of the shear strengthened beams
b_{sp}	span of the beam which has no shear strengthened CFRP laminates
θ_f	CFRP inclination with respect to the longitudinal axis of the beam
ρ_{sw}	ratio of steel stirrups for the beams
ρ_{sl}	ratio of tensile steel bars for the beams
ρ_f	shear strengthening ratio of the beams

712

Table captions

713

Figure captions

Fig. 9 Prediction of the PDSC model for closing a crack developed in one direction, by imposing compressive load in the orthogonal direction (Values for the parameters of the constitutive model: $\nu = 0.2$; $E = 33GPa$; $f_c = 30MPa$; $G_{f,c} = 30N/mm$; $f_{ct} = 2.45MPa$; $\varepsilon_{c1} = 0.0022$; $\alpha_0 = 0.3$; $G_f^{\mathrm{I}} = 0.05N/mm$, $\xi_1 = 0.2; \alpha_1 = 0.7$, $\xi_2 = 0.75, \alpha_2 = 0.2$.

Fig. 10 Simulation of the S4 shear wall tested by Maier and Thürlimann [39]: (a) geometry and loading configurations (dimensions in *mm*) ; (b) finite element mesh used for the analysis; (c) horizontal load versus horizontal displacement diagram, F_h-U_h; (d) experimentally observed crack pattern [39]; (e) crack pattern and (f) plastic zone at $U_h \approx 18mm$ (final converged step).

Fig. 11 Simulation of the S1 shear wall, tested by Maier and Thürlimann [39] by PDSC model and assuming $G_{f,c} = 30N/mm$: (a) geometry and loading configurations (dimensions in *mm*) ; (b) finite element mesh; (c) horizontal load versus horizontal displacement diagram, F_h-U_h; (d) experimentally observed crack pattern [39]; (e) numerical crack pattern; (f) numerical plastic zone (results of (e) and (f) correspond to $U_h \approx 30mm$, the final converged step).

Fig. 12 Uniaxial constitutive model (for both tension and compression) for the steel bars [22].

Fig. 13 Geometry of the reference beam (3S-R), steel reinforcements common to all beams, support and load conditions (dimensions in mm) [41].

Fig. 14 NSM shear strengthening configurations (CFRP laminates at dashed lines; dimensions in mm) [41].

Fig. 15 Finite element mesh used for the beam 3S-4LI-S2 (dimensions are in mm).

Fig. 16 Experimental [41] and numerical load versus the deflection at loaded deflection: (a) 3S-R; (b) 3S-4LI-S2; (c) 3S-4LI-P2; (d) 3S-4LI4LI-SP1; (e) 3S-4LI4LV-SP1.

Fig. 17 Crack patterns of the tested beams at failure [41].

Fig. 18 The crack patterns and plastic zone predicted by PDSCM model for the beams at the experimental: (a) 3S-R; (b) 3S-4LI-S2; (c) 3S-4LI-P2; (d) 3S-4LI4LI-SP1; (e) 3S-4LI4LV-SP1. (Note: the results are correspondent to the final converged step).

Fig. A.1 Willam-Warnke failure surface represented in (a) meridian plane; (b) deviatoric plane ($\bar{\sigma}_1, \bar{\sigma}_2, \bar{\sigma}_3$ are the principle stresses in the effective stress space).

Fig. B.1 Cyclic uniaxial compressive test of Karsan and Jirsa [37]; (a) the $\bar{\sigma}_c - \tilde{\epsilon}_c$ law of the model, (b) Experimental [39] versus predicted stress-strain response (assuming $l_0 = 4.5$).

714

715

716

717

718 **VITAE**

Author	Author's name	Photo	Biography
1	**Ali Edalat Behbahani**		**Ali Edalat Behbahani** is a PhD student at ISISE, Department of Civil Engineering, School of Engineering, University of Minho, Campus de Azurém, Guimarães, Portugal. His research interests include constitutive modelling, and FEM based analysis of concrete and RC structures.
2	**Joaquim António Oliveira de Barros**		**Joaquim António Oliveira de Barros** is a full professor at ISISE, Department of Civil Engineering, School of Engineering, University of Minho, Campus de Azurém, Guimarães, Portugal. Main scientific area of research: - Numerical models for the material and geometrical nonlinear analysis of concrete structures and structures strengthened by composite materials; - Experimental research to characterize the behaviour of cement based materials, mainly fibre reinforced concrete, fibre reinforced self-compacting concrete and engineering cement composite; - Structural rehabilitation.
3	**António Ventura-Gouveia**		**António Ventura-Gouveia** is an adjunct professor at ISISE, Department of Civil Engineering, School of Technology and Management of Viseu, Polytechnic Institute of Viseu, Viseu, Portugal. His research interest includes: computational modelling; fiber reinforced concrete; time dependent phenomenon; and strengthening techniques.

719

720

721

722 Table 1 – Values of the parameters of the concrete constitutive model for shear wall test.

Property	Value
Poisson's ratio (ν)	0.15
Young's modulus (E)	26000 N/mm^2
Compressive strength (f_c)	30.0 N/mm^2
Strain at compression peak stress (ε_{c1})	0.0035
Compressive fracture energy ($G_{f,c}$)	for the wall S4 20, 30, 40 N/mm ; for the wall S1 30 N/mm
Parameter to define elastic limit state (α_0)	0.4
Trilinear tension-softening diagram	$f_{ct} = 2.2\,N/mm^2; G_f^{\mathrm{I}} = 0.14\,N/mm; \xi_1 = 0.15; \alpha_1 = 0.3; \xi_2 = 0.575; \alpha_2 = 0.15$
Parameter defining the mode I fracture energy available to the new crack [22]	2
Type of shear retention factor law	$P_1 = 2$
Crack bandwidth	Square root of the area of Gauss integration point
Threshold angle [22]	30 degree
Maximum number of cracks per integration point [22]	2

723

724

725

726

727

728

729

730

731

732

733

734

735

736

737

738

739

740

741

742

743 Table 2 – Values of the parameters of the steel constitutive model for shear wall test.

	$\varepsilon_{sy}(\%)$	$\sigma_{sy}(N/mm^2)$	$\varepsilon_{sh}(\%)$	$\sigma_{sh}(N/mm^2)$	$\varepsilon_{su}(\%)$	$\sigma_{su}(N/mm^2)$	Third branch exponent
$\phi 8$	0.287	574	0.287	574	2.46	764	1

744
745
746
747
748
749
750
751
752
753
754
755
756
757
758
759
760
761
762
763
764
765
766
767
768
769
770
771
772

Table 3 - General information about the series of the tested RC beams.

Beam	ρ_{sl} [%]	ρ_f [%]	θ_f [°]	ρ_{sw} [%]	f_c [MPa]	a_{sp}/d (1)
3S-4LI-S2	2.0	0.113	52	0.09	40.1	2.5
3S-4LI-P2		0.113	52			
3S-4LI4LI-SP1		0.113	52			
3S-4LI4LV-SP1		0.101	52/90			

(1) d: effective depth

Table 4 - CFRP shear strengthening configurations of the tested beams.

Beam	Shear reinforcement system in the shear span a_{sp}				
	Material	Quantity	Percentage [%]	Spacing [mm]	Angle [º]
3S-4LI-S2	Steel stirrups	3ϕ6	0.09	350	90
	NSM CFRP laminates	2×4 laminates (1.4×20 mm^2)	0.113	350	52
3S-4LI-P2	Steel stirrups	3ϕ6	0.09	350	90
	NSM CFRP laminates	2×4 laminates (1.4×20 mm^2)	0.113	350	52
3S-4LI4LI-SP1	Steel stirrups	3ϕ6	0.09	350	90
	NSM CFRP laminates	2×(4×2) laminates (1.4×10 mm^2)	0.113	350	52
3S-4LI4LV-SP1	Steel stirrups	3ϕ6	0.09	350	90
	NSM CFRP laminates	2×4 laminates (1.4×10 mm^2)	0.056	350	90
	NSM CFRP laminates	2×4 laminates (1.4×10 mm^2)	0.044	350	52

Table 5 – Values of the parameters of the steel constitutive model for RC beams failing in shear.

Property	$\phi 6$	$\phi 10$	$\phi 12$	$\phi 16$	$\phi 32$
$\varepsilon_{sy}(\%)$	0.27805	0.2833	0.2833	0.2804	0.32725
$\sigma_{sy}(N/mm^2)$	556.1	566.6	566.6	560.8	654.5
$\varepsilon_{sh}(\%)$	1	1	1	1	1
$\sigma_{sh}(N/mm^2)$	583.905	594.93	594.93	588.8	687.2
$\varepsilon_{su}(\%)$	10	10	10	10	10
$\sigma_{su}(N/mm^2)$	682.6	661.6	661.6	675.0	781.9
Third branch exponent	1	1	1	1	1

841 Table 6 – Values of the parameters of the concrete constitutive model for RC beams failing in shear.

Property	Value
Poisson's ratio (ν)	0.15
Young's modulus (E)	32000 N/mm^2
Compressive strength (f_c)	for strengthened beams $f_c = 40.1 N/mm^2$; for the reference beam (3S_R) $f_c = 36.4 N/mm^2$
Strain at compression peak stress (ε_{c1})	0.0035
Compressive fracture energy ($G_{f,c}$)	20 N/mm
Parameter to define elastic limit state (α_0)	0.4
Trilinear tension-softening diagram	$f_{ct} = 2.5 N/mm^2; G_f^1 = 0.1 N/mm; \xi_1 = 0.008; \alpha_1 = 0.25; \xi_2 = 0.4; \alpha_2 = 0.05$
Parameter defining the mode I fracture energy available to the new crack [22]	2
Crack shear stress-crack shear strain softening diagram	$\tau_{t,p}^{cr} = 1.6 N/mm^2; \beta = 0.03$ for strengthened beams $G_{f,s} = 0.3 N/mm$; for the reference beam (3S_R) $G_{f,s} = 0.04 N/mm$;
Crack bandwidth	square root of the area of Gauss integration point
Threshold angle [22]	30 degree
Maximum number of cracks per integration point [22]	2

842

843

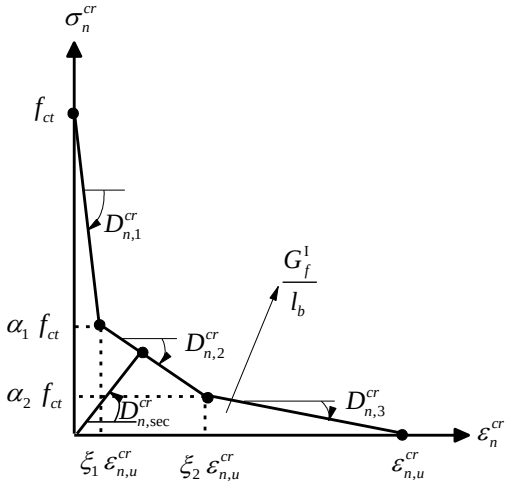

Fig. 1 – Diagram for modelling the fracture mode I at the crack coordinate system [22].

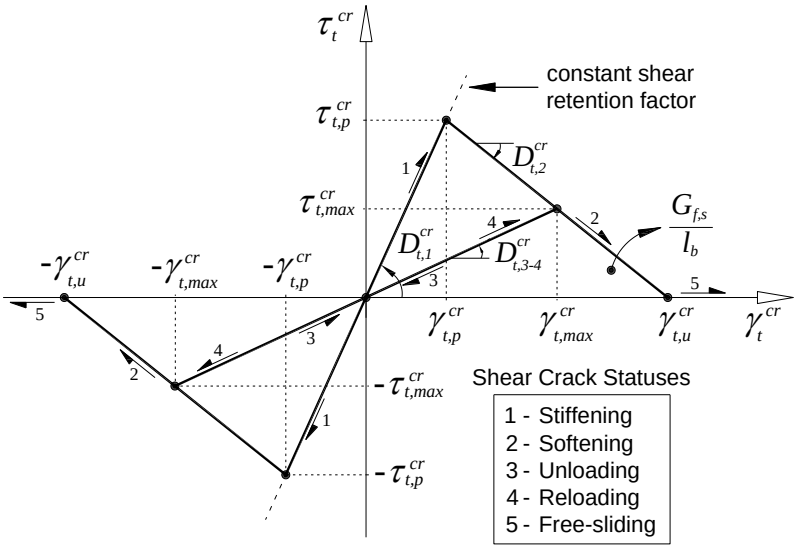

Fig. 2 – Diagram for modelling the fracture mode II at the crack coordinate system [23].

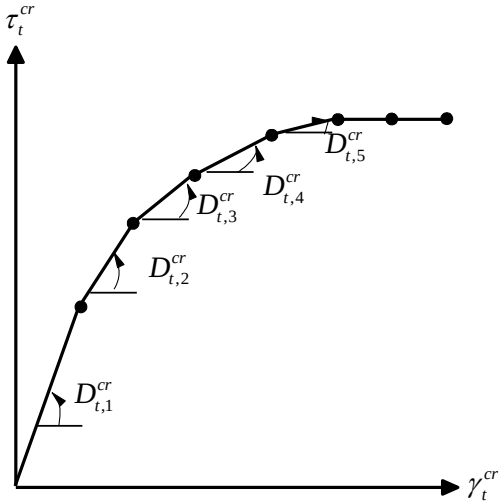

Fig. 3 – Relation between crack shear stress and crack shear strain for the incremental approach based on a shear retention factor [22].

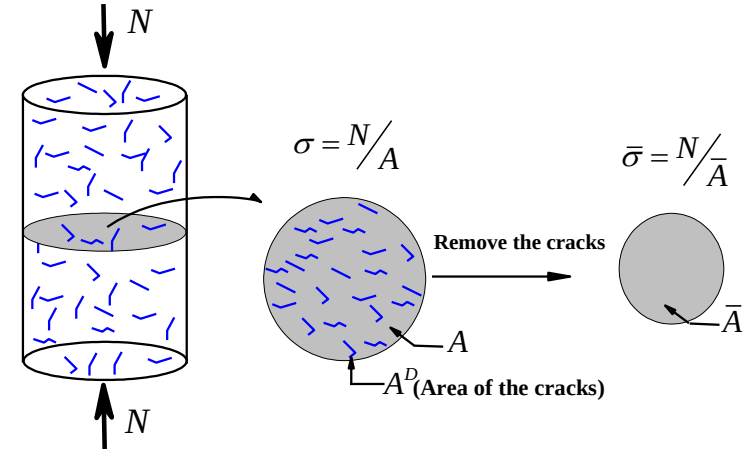

(a) the bar under compression (b) Nominal (damaded) configuration (c) Effective (undamaded) configuration

Fig. 4 – One dimensional representation of the effective and nominal stresses [14].

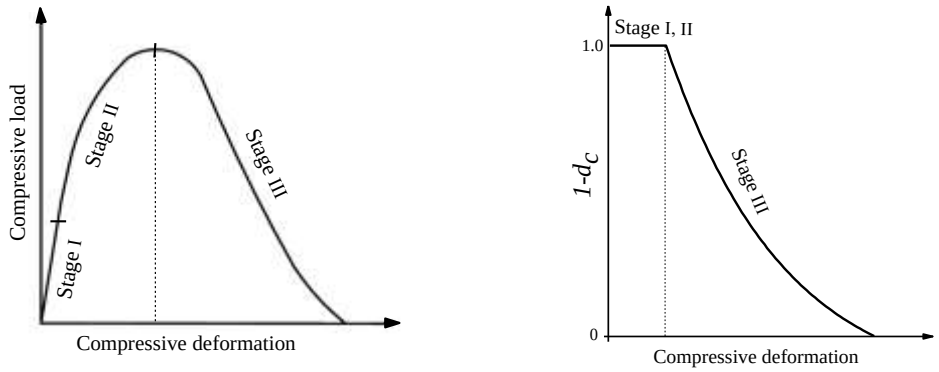

(a) (b)

Fig. 5 – Behaviour of the cement based materials under uniaxial compression: (a) three stage of cracking [27], (b) schematic representation of damage evolution in the proposed model.

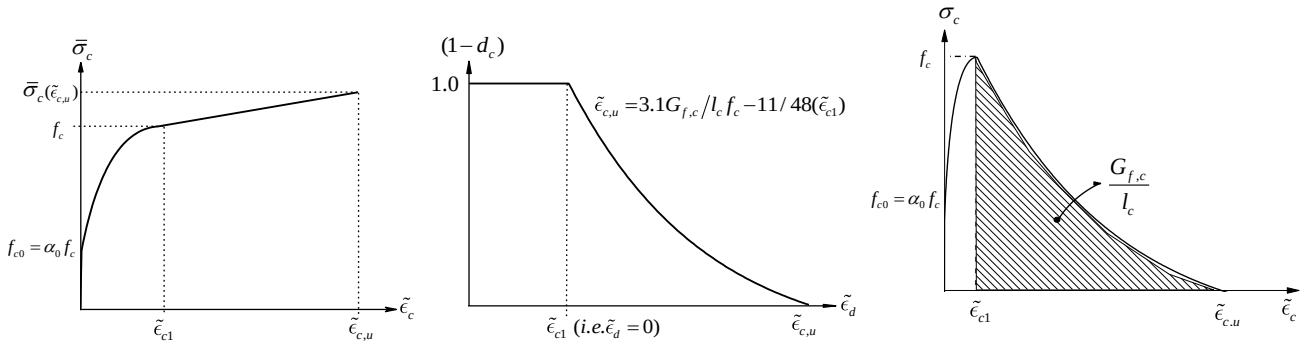

Fig. 6 – Diagrams for modelling compression: (a) the $\bar{\sigma}_c - \tilde{\epsilon}_c$ relation (in effective stress space) used in the proposed plasticity model; (b) the $(1-d_c)-\tilde{\epsilon}_d$ relation adopted in isotropic damage model; (c) the $\sigma_c - \tilde{\epsilon}_c$ diagram for compression with indication of the compressive fracture energy, $G_{f,c}$.

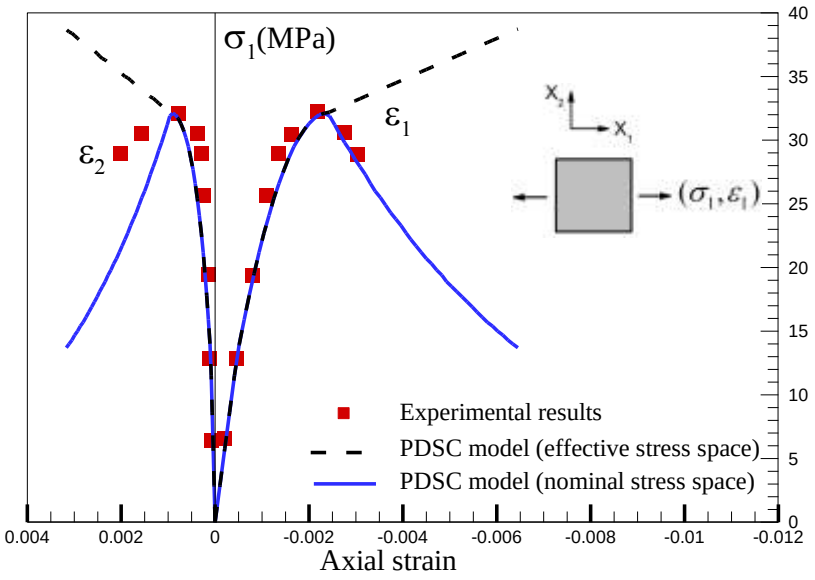

Fig. 7 – Experimental [36] versus predicted stress-strain response of concrete under monotonic uniaxial compressive test: (Values for the parameters of the constitutive model: poison's ratio, $\nu = 0.2$; young's modulus, $E = 27GPa$; compressive strength, $f_c = 32\,MPa$; strain at compression peak stress $\varepsilon_{c1} = 0.0023$; parameter to define elastic limit state $\alpha_0 = 0.3$; compressive fracture energy, $G_{f,c} = 15.1N/mm$).

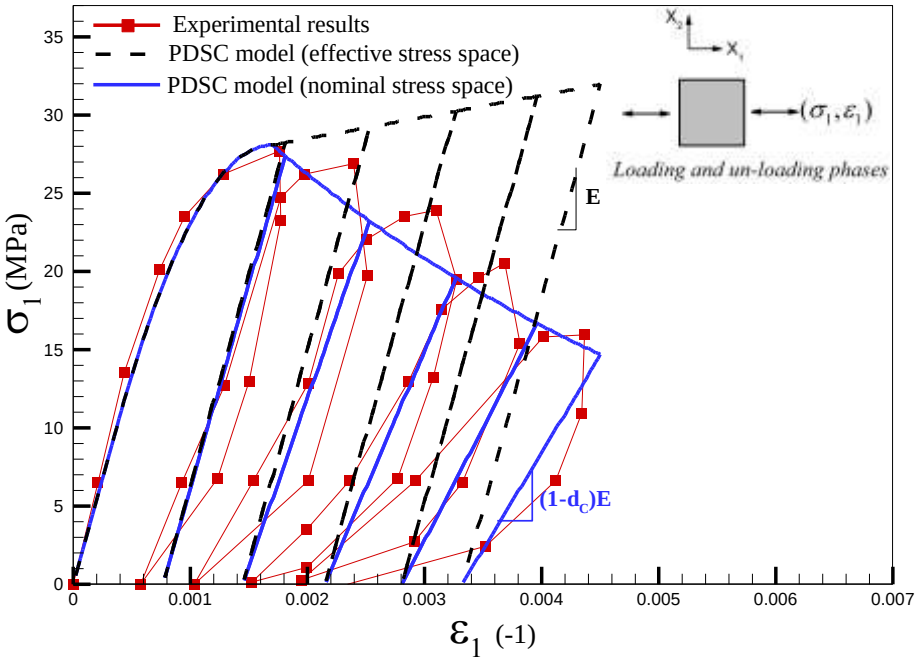

Fig. 8 – Experimental [37] versus predicted stress-strain response of concrete under cyclic uniaxial compressive test: (Values for the parameters of the constitutive model: $\nu = 0.2$; $E = 27 GPa$; $\alpha_0 = 0.3$; $\varepsilon_{c1} = 0.0017$; $f_c = 28 MPa$; $G_{f,c} = 11.5 N/mm$).

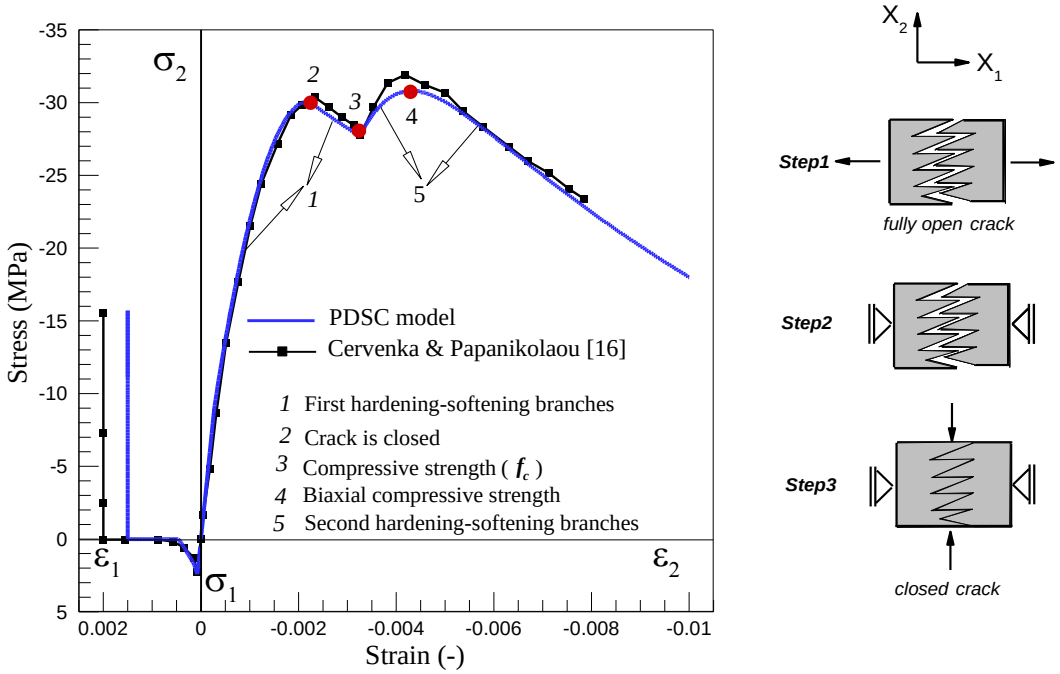

Fig. 9 – Prediction of the PDSC model for closing a crack developed in one direction, by imposing compressive load in the orthogonal direction (Values for the parameters of the constitutive model: $\nu = 0.2$; $E = 33GPa$; $f_c = 30\,MPa$; $G_{f,c} = 30\,N/mm$; $f_{ct} = 2.45\,MPa$; $\varepsilon_{c1} = 0.0022$; $\alpha_0 = 0.3$; $G_f^1 = 0.05\,N/mm$, $\xi_1 = 0.2; \alpha_1 = 0.7; \xi_2 = 0.75; \alpha_2 = 0.2$.

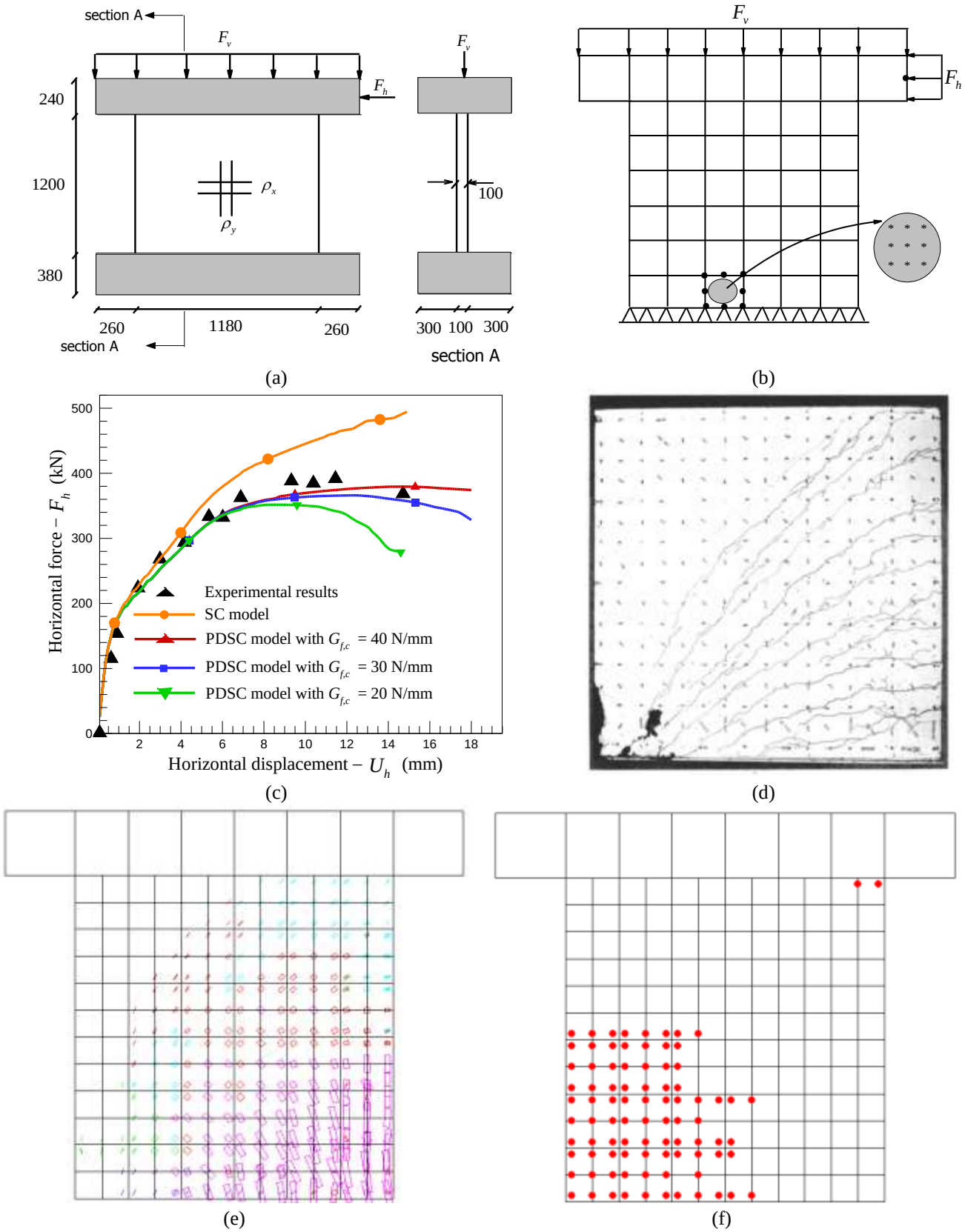

Fig. 10 – Simulation of the S4 shear wall tested by Maier and Thürlimann [39]: (a) geometry and loading configurations (dimensions in mm); (b) finite element mesh used for the analysis; (c) horizontal load versus horizontal displacement diagram, F_h-U_h; (d) experimentally observed crack pattern [39]; (e) crack pattern and (f) plastic zone (results of (e) and (f) correspond to $U_h \approx 18\,mm$, the final converged step).

(In pink color: crack completely open; in red color: crack in the opening process; in cyan color: crack in the reopening process; in green color: crack in the closing process; in blue color: closed crack; in red circle: the plastic zone).

1017

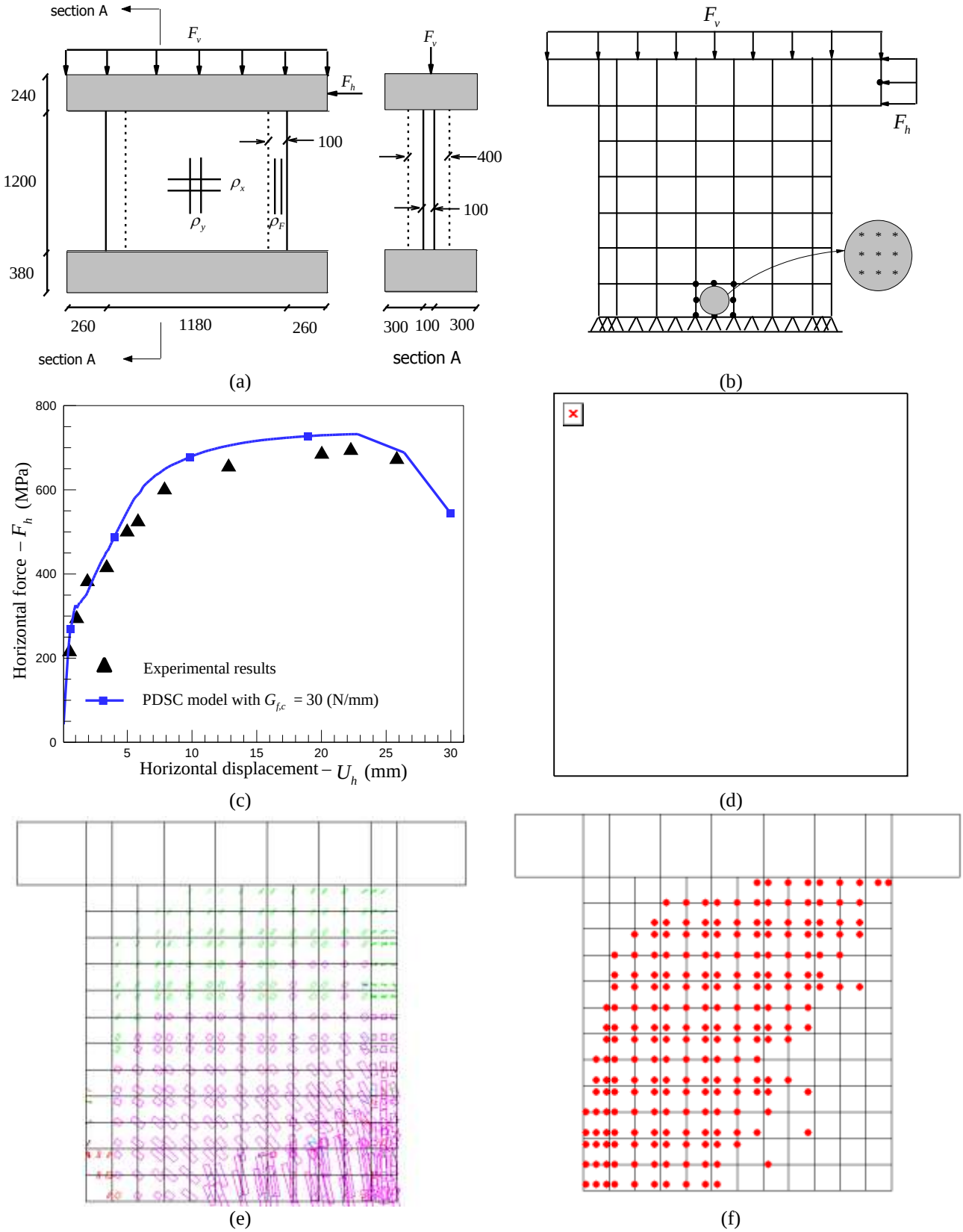

Fig. 11 – Simulation of the S1 shear wall, tested by Maier and Thürlimann [39] by PDSC model and assuming $G_{f,c} = 30\,N/mm$: (a) geometry and loading configurations (dimensions in mm) ; (b) finite element mesh; (c) horizontal load versus horizontal displacement diagram, F_h-U_h; (d) experimentally observed crack pattern [39]; (e) numerical crack pattern; (f) numerical plastic zone (results of (e) and (f) correspond to $U_h \approx 30\,mm$, the final converged step).

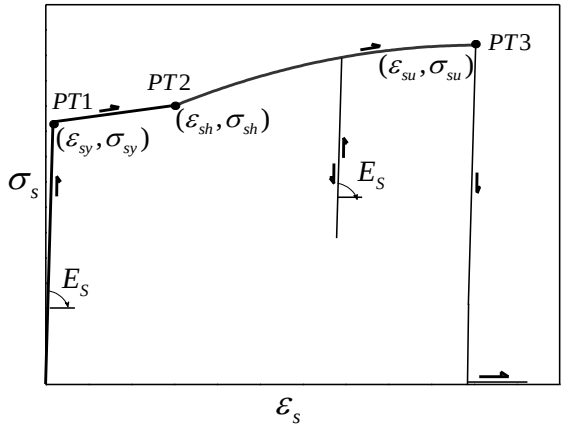

Fig. 12 – Uniaxial constitutive model (for both tension and compression) for the steel bars [22].

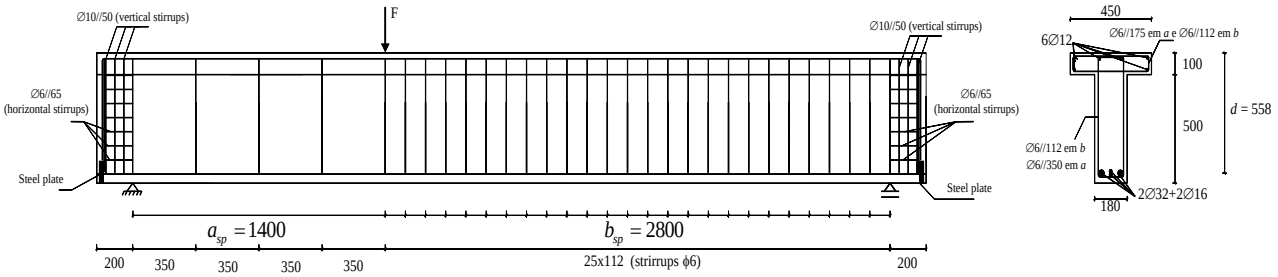

Fig. 13 - Geometry of the reference beam (3S-R), steel reinforcements common to all beams, support and load conditions (dimensions in mm) [41].

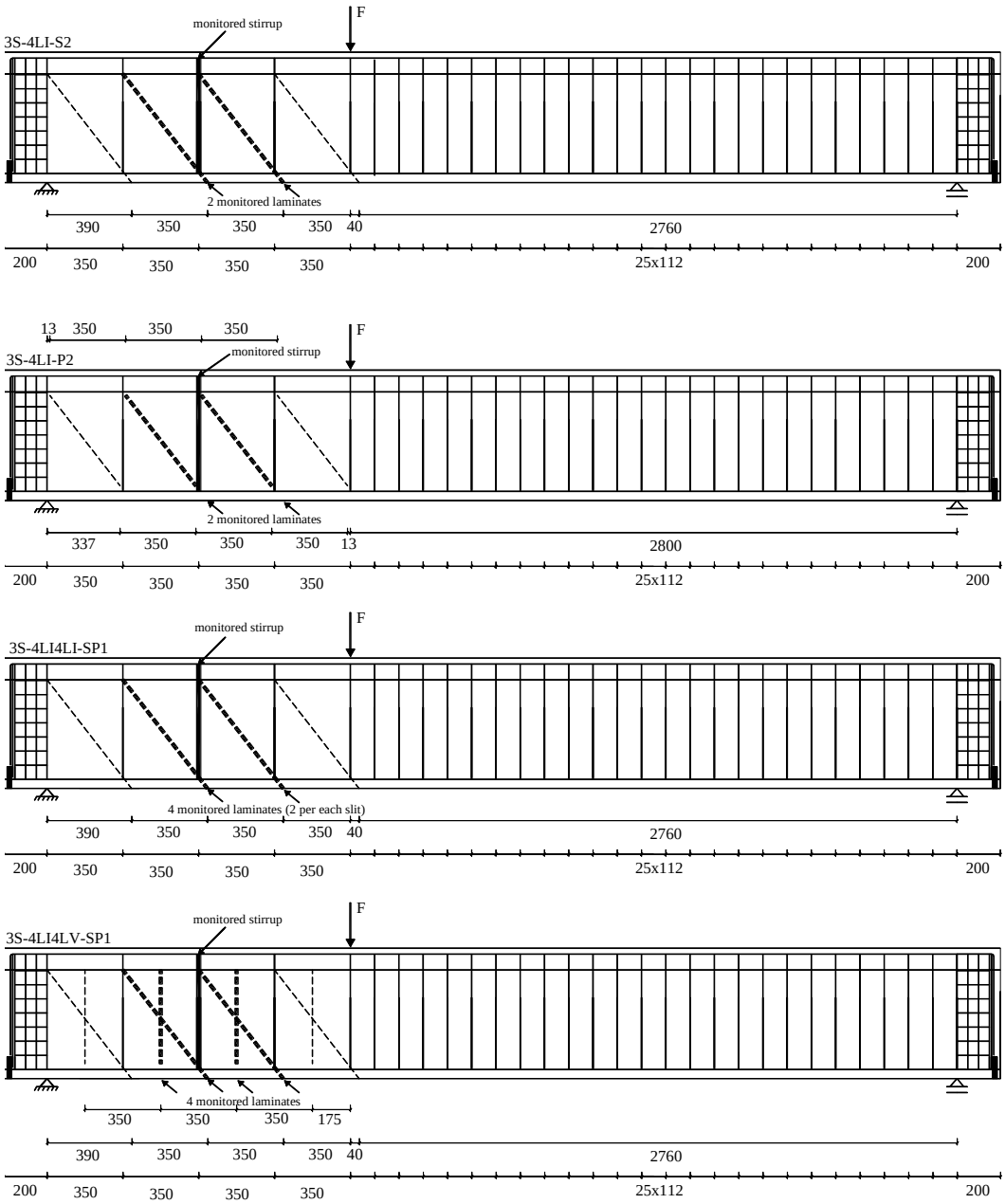

Fig. 14 – NSM shear strengthening configurations (CFRP laminates at dashed lines; dimensions in mm) [41].

1067

1068

1069

1070

1071

1072

1073

1074

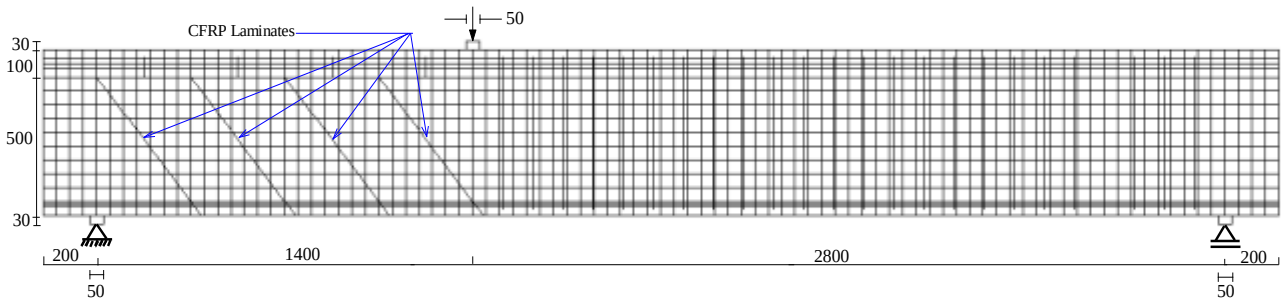

Fig. 15 – Finite element mesh used for the beam 3S-4LI-S2 (dimensions are in mm).

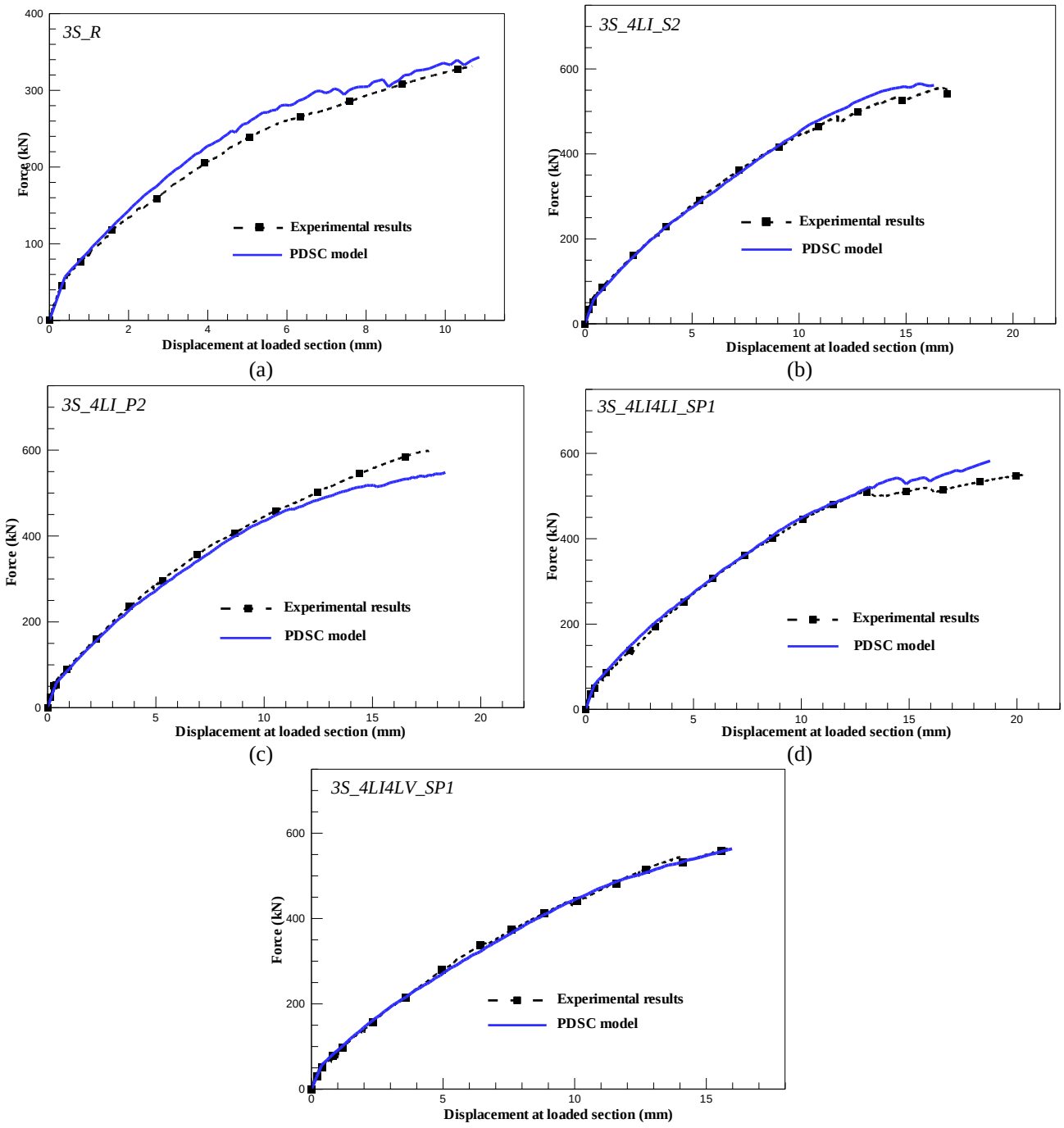

Fig. 16 – Experimental [41] and numerical load versus the deflection at loaded deflection: (a) 3S-R; (b) 3S-4LI-S2; (c) 3S-4LI-P2; (d) 3S-4LI4LI-SP1; (e) 3S-4LI4LV-SP1.

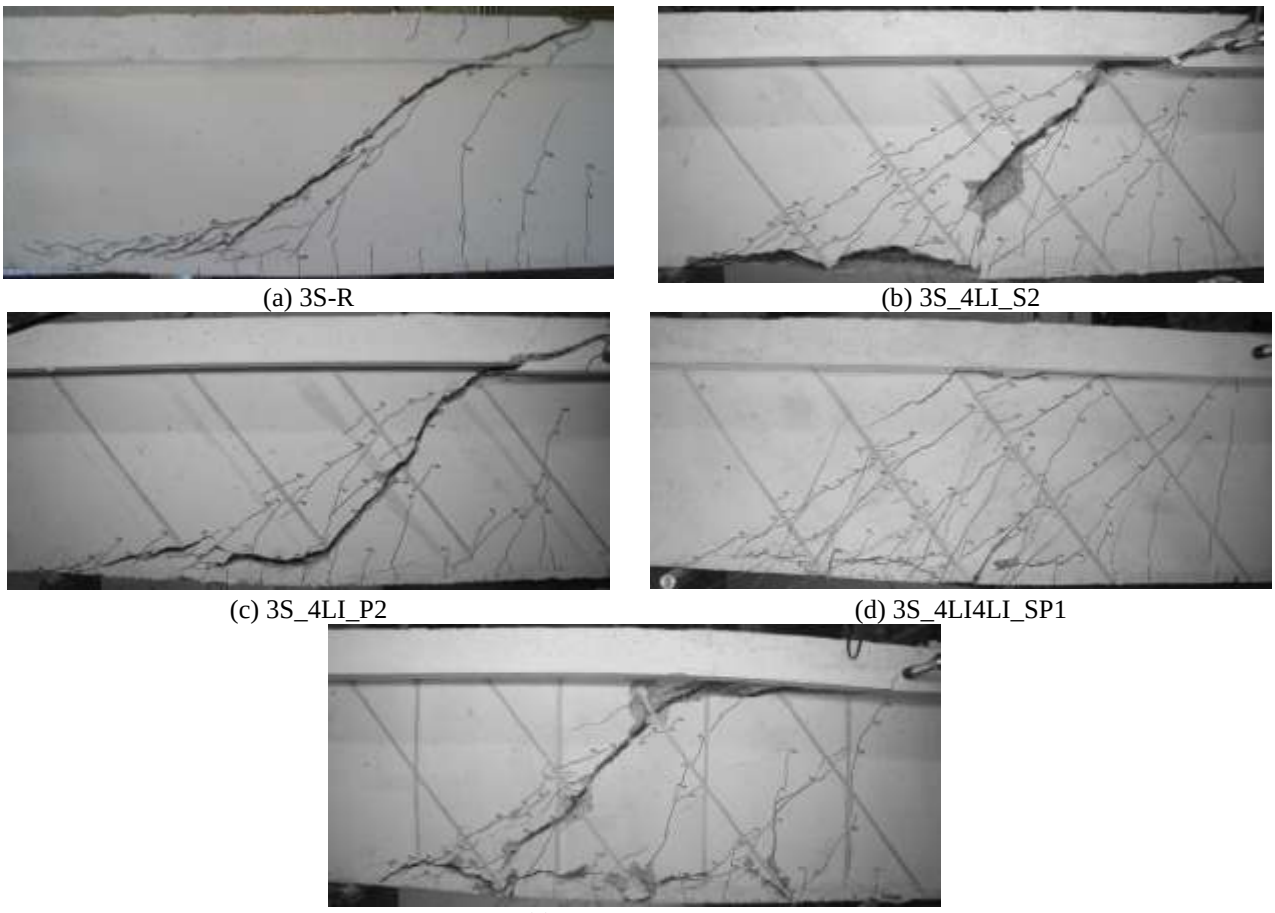

(a) 3S-R (b) 3S_4LI_S2

(c) 3S_4LI_P2 (d) 3S_4LI4LI_SP1

(e) 3S_4LI4LV_SP1

Fig. 17 – Crack patterns of the tested beams at failure [41].

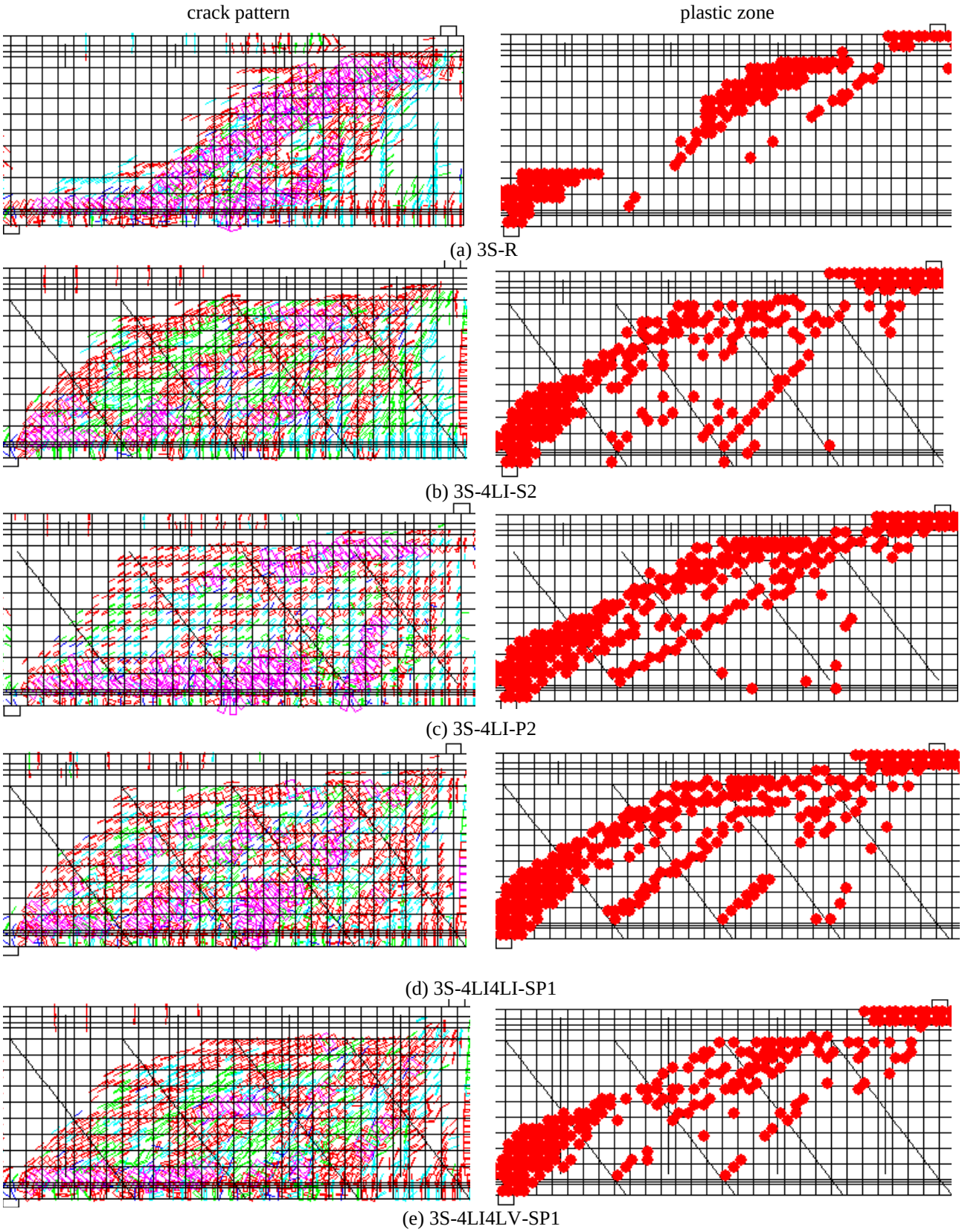

Fig. 18 – The crack patterns and plastic zone predicted by PDSC model for the beams at the experimental: (a) 3S-R; (b) 3S-4LI-S2; (c) 3S-4LI-P2; (d) 3S-4LI4LI-SP1; (e) 3S-4LI4LV-SP1 (the results are correspondent to the final converged step).
(In pink color: crack completely open; in red color: crack in the opening process; in cyan color: crack in the reopening process; in green color: crack in the closing process; in blue color: closed crack; in red circle: the plastic zone).

1123

1124

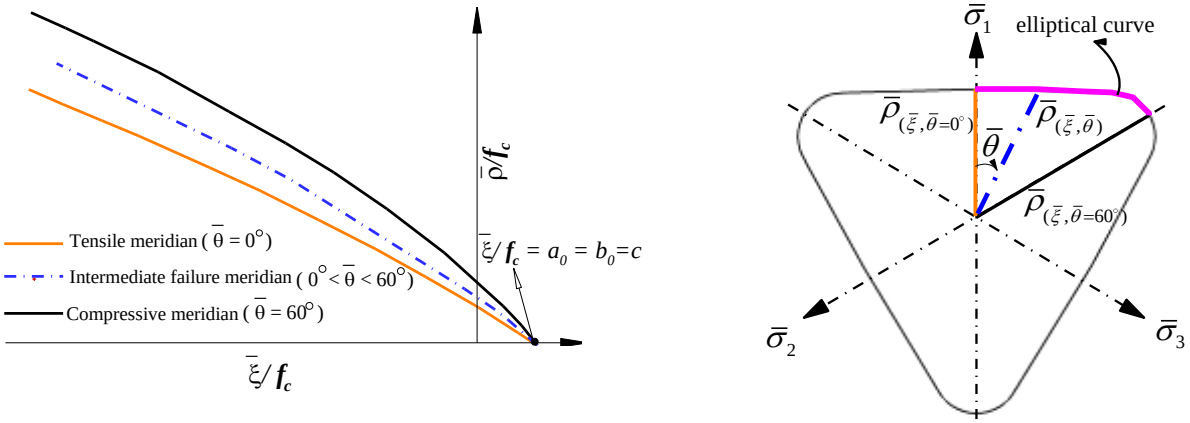

(a) (b)

Fig. A.1 – Willam-Warnke failure surface represented in (a) meridian plane; (b) deviatoric plane ($\bar{\sigma}_1, \bar{\sigma}_2, \bar{\sigma}_3$ are the principle stresses in the effective stress space).

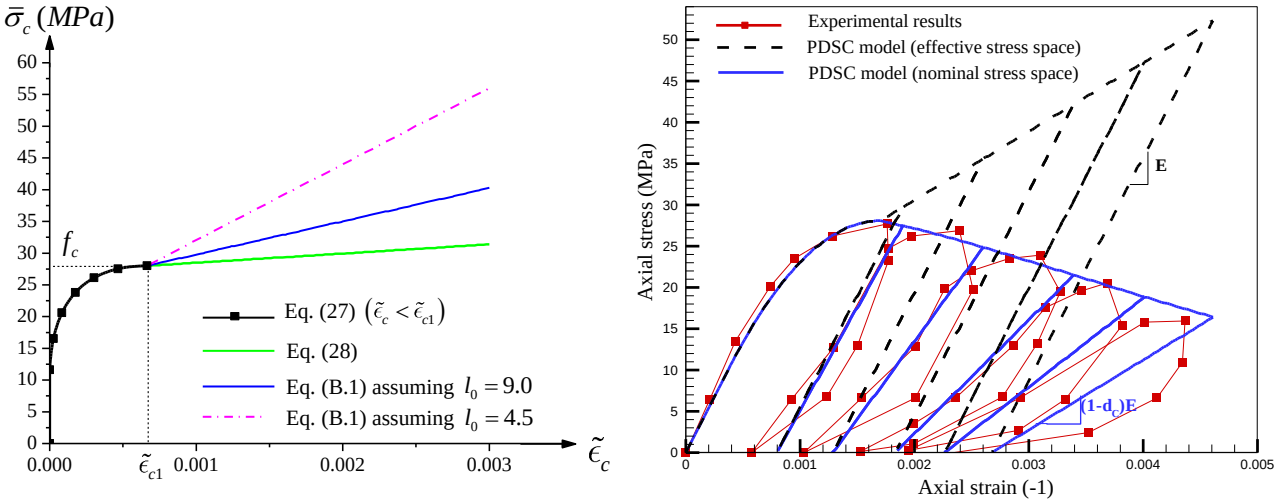

(a) (b)

Fig. B.1 – Cyclic uniaxial compressive test of Karsan and Jirsa [37]; (a) the $\bar{\sigma}_c - \tilde{\epsilon}_c$ law of the model, (b) Experimental [39] versus predicted stress-strain response (assuming $l_0 = 4.5$).